XIII. PLASMAS AND CONTROLLED NUCLEAR FUSION

A. Active Plasma Systems*

Academic and Research Staff

Prof. L. D. Smullin
Prof. A. Bers
Prof. R. J. Briggs
Prof. J. G. Siambis

Graduate Students

R. R. Bartsch
S. R. J. Brueck
S-L. Chou
J. A. Davis
F. N. Herba
B. R. Kusse
O. Lopez
J. A. Mangano
R. R. Parker
D. M. Perozek
H. M. Schneider
R. E. Tremain, Jr.
R. N. Wallace

1. SYSTEM C: EXCITATION OF AN ION-CYCLOTRON RESONANCE

A method of exciting ion-cyclotron resonance by modulation of the electron beam normally used to create a beam-plasma discharge has been proposed.[1] This method of excitation is being investigated experimentally in System C. An RF pulse transformer has been used to modulate the 8-kV DC beam pulse with 4-kV peak-to-peak of

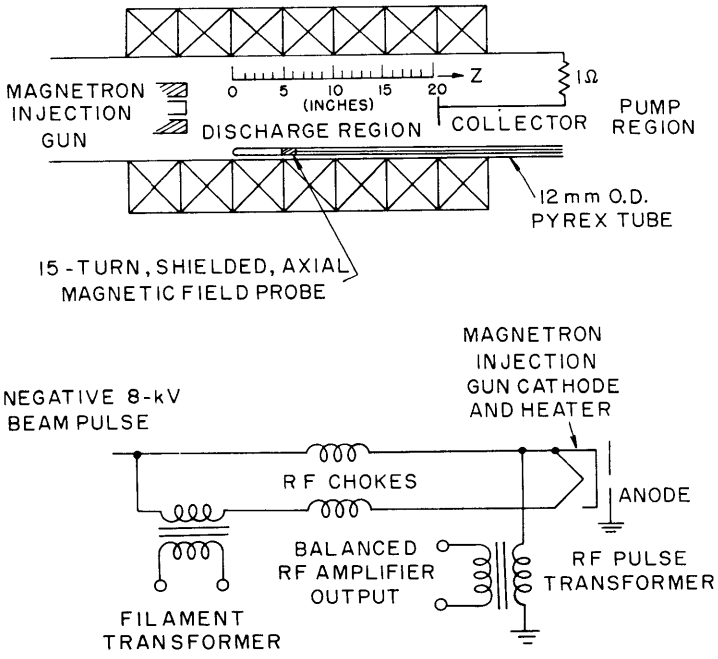

Fig. XIII-1. Upper: drift tube showing probe position and coordinate system. Lower: beam-pulse modulation circuit.

*This work was supported by the National Science Foundation (Grants GK-57 and GK-1165).

RF voltage. The circuit is shown schematically in Fig. XIII-1. The driver and balanced output stages of an RF amplifier (10 kW) is keyed to provide an RF pulse of variable width and starting time. Under normal operating conditions, an RF pulse of 350-μsec duration is turned on 150 μsec after the beginning of the DC beam pulse (Fig. XIII-2). The width of the negative DC beam pulse is 700 μsec, with a repetition rate of 2/sec. The modulation frequency may be varied continuously over the range 1-4 MHz. With the present magnet coil configuration, the axial static magnetic field may be adjusted smoothly from a 2000-Gauss uniform field to a mirror field with a midplane intensity of 1000 Gauss and a mirror ratio of 2. For the experimental data reported, the beam-plasma discharge is generated in hydrogen gas at pressures from 7×10^{-5} Torr to 2×10^{-4} Torr.

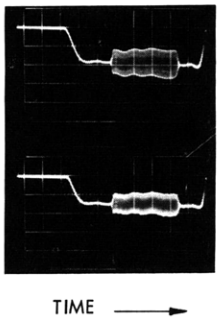

Fig. XIII-2.

Beam voltage with and without a beam-plasma discharge. Voltage scale, 4 kV/cm; time scale, 0.1 msec/cm; modulation frequency, 2.0 MHz. (a) V_b no plasma discharge. (b) V_n with beam-plasma discharge.

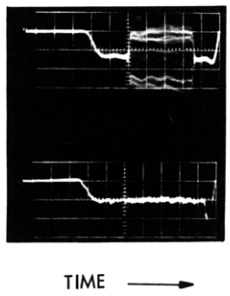

Fig. XIII-3.

Current scale, 2 amps/cm; time scale, 0.1 msec/cm.
(a) Collector current with no hydrogen gas in the system (no beam-plasma discharge).
(b) Collector current with 1.0 Torr of hydrogen gas in the system (with beam-plasma discharge).

With no hydrogen gas admitted into the system, a measurement of the collector current indicates nearly 100% RF modulation of the DC current pulse of 7 amps (Fig. XIII-3). When gas is admitted to the system and a beam-plasma discharge created, the RF modulation of the cathode current is substantially unchanged, but the collector RF current is reduced by approximately a factor of 15.

Since we are looking for a resonance of the cyclotron motion of the plasma ions, relatively large azimuthal currents are expected. These currents will produce an axial RF magnetic field that should be resonant at the ion-cyclotron frequency. Therefore a movable, electrostatically shielded, magnetic-field probe has been inserted near the drift tube wall to measure resonance effects in the axial RF field (Fig. XIII-1). The

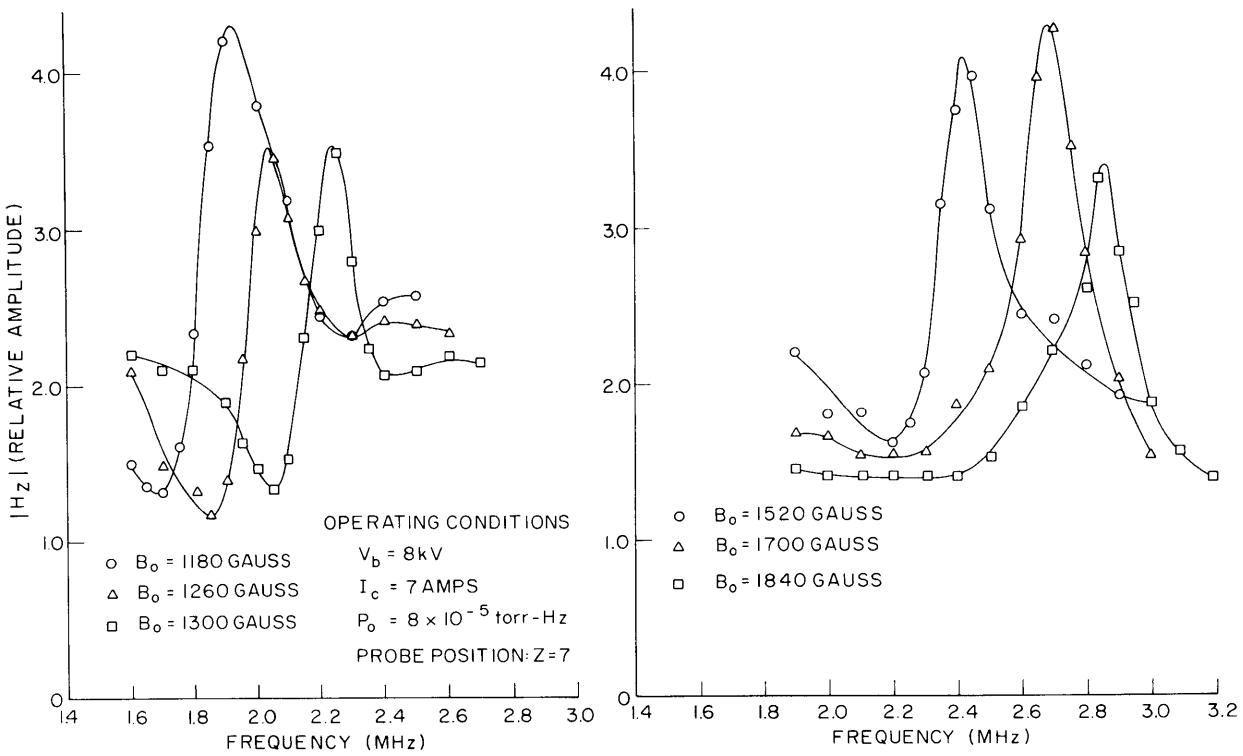

Fig. XIII-4. Axial magnetic probe signal as a function of frequency.

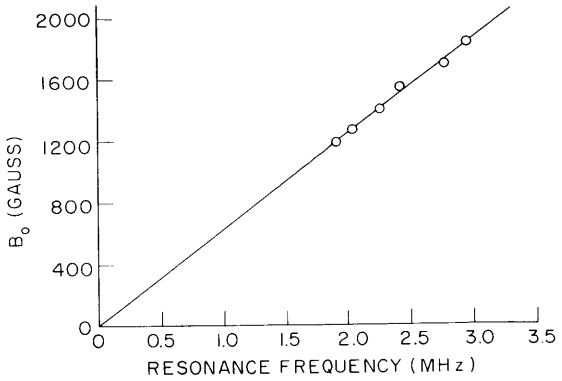

Fig. XIII-5. Known magnetic field at z = 7 inches, vs measured resonant frequencies.

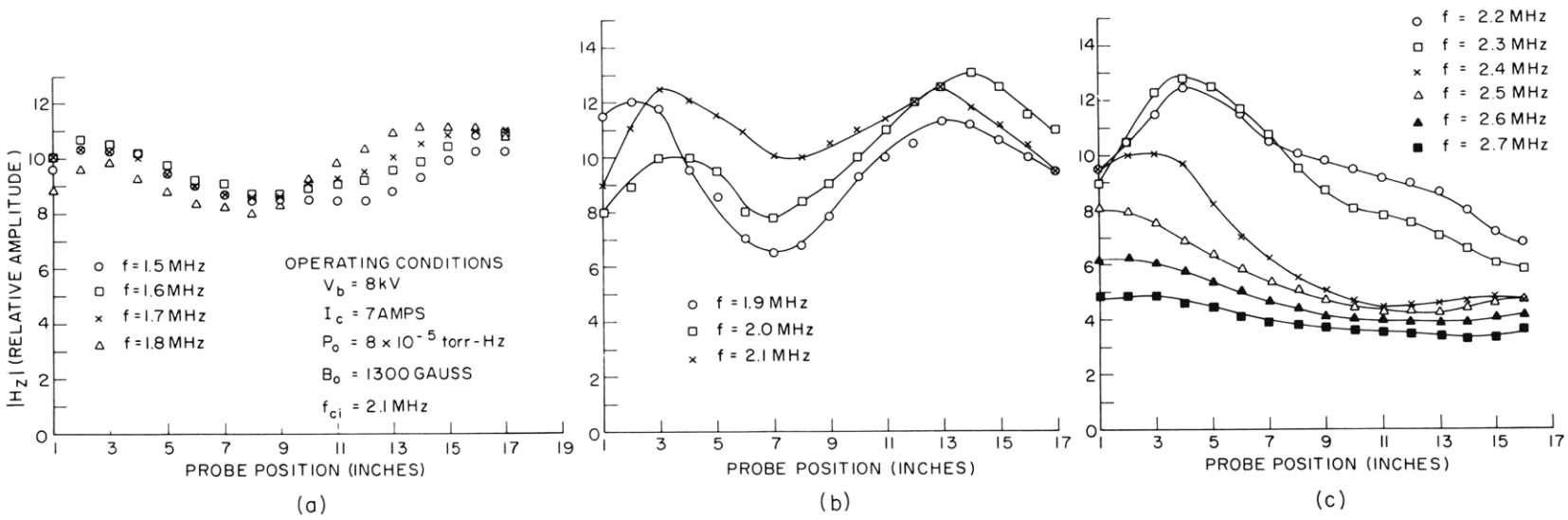

Fig. XIII-6. Axial variation of $|H_z|$. (a) at frequencies below f_{ci}. (b) at frequencies near f_{ci}. (c) at frequencies above f_{ci}.

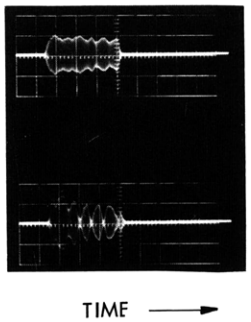

Fig. XIII-7. Filtered H_z probe signal. Vertical scale, 0.05 volts/cm; time scale, 0.1 msec/cm.
(a) Typical signal away from resonance.
(b) Typical signal just before resonance is reached.

output of the probe is filtered, peak-detected, and integrated. Basically, two types of measurements have been made with this probe. The amplitude of H_z has been measured in two ways: (a) at a fixed position in the drift tube with the magnetic field and frequency as varying parameters, and (b) in a fixed magnetic field with the frequency and probe position as parameters.

The results of these measurements are shown in Figs. XIII-4, XIII-5, and XIII-6. Figure XIII-4 is a plot of the H_z probe signal, taken at a fixed position, as a function of frequency. The magnetic field at the probe position is varied over a range from 1180 Gauss to 1840 Gauss. In this experiment, the region from z = 1 to z = 15 (see (Fig. XIII-1) has an essentially uniform field; however, the current in the magnets at each end of the system is chosen to maintain a field of 1900 Gauss under these magnets. Therefore as the magnetic field at the probe position is increased, the mirror ratio is reduced. When a uniform field over the entire length of the system is used, the magnitude of the resonance is reduced by a factor of 2. Figure XIII-5 is a plot of the observed resonance frequencies versus the known magnetic field. These data are taken from Fig. XIII-4. Figure XIII-6 is a plot of the axial variation of the H_z probe signal for frequencies from 1.5 MHz to 2.7 MHz. The magnetic field is essentially uniform and equal to 1300 Gauss from z = 1 to z = 15. Again, the current in the end magnet was chosen to operate with a field of 1900 Gauss directly under these magnets. Figure XIII-7 illustrates the change in the structure of the RF H_z field as the resonant frequency is approached.

The method by which the modulated electron beam couples energy to the plasma ions is, at present, not understood. Theoretical work is being done which may explain the central role played by the nonuniform field in the excitation of the resonance, and the axial variation of the H_z signal.

J. A. Mangano

References

1. L. D. Smullin, "Beam-Plasma Discharge: Excitation of Ions at the Ion-Cyclotron Frequency," Quarterly Progress Report No. 80, Research Laboratory of Electronics, M.I.T., January 15, 1966, pp. 111-113.

2. BEAM-PLASMA DISCHARGE: SYSTEM D

The x-ray Bremsstrahlung spectrum has been measured during the afterglow of the beam-plasma discharge. A thin-window sodium iodide scintillation crystal, 2 inches in diameter, has been used with an RIDL pulse-height analyzer and photomultiplier. The detection crystal is shielded and collimated so that only the emission of the core of the discharge is observed. The vacuum window between the scintillation crystal and the discharge is a thin beryllium disc (~5 mils).

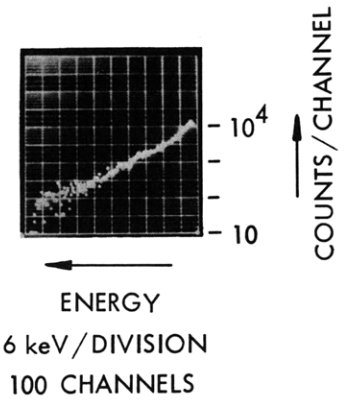

Fig. XIII-8. X-ray spectrum, 0.4-2.7 msec after the beam-plasma discharge (30 minutes at 30 discharges/minute).

The pulse-height analyzer is gated at various times during the afterglow. A typical x-ray spectrum is shown in Fig. XIII-8. We have used the Fessenden's model for Bremsstrahlung in nonrelativistic Coulomb collisions to determine the electron density during the afterglow (the plasma temperature can be read directly from the observed spectrum).[1] The plasma energy density ($n_e T_e$) as determined from the x-ray measurements is shown in Fig. XIII-9, where we have also shown the decay of the diamagnetism (transverse energy density) as observed by a pickup coil inside the discharge tube. Data are shown for pressures up to 10 times the normal operating pressure. The diamagnetic and x-ray measurements of the plasma energy density are in agreement at the higher pressures. We interpret the disagreement at the lower pressures as being attributable to enhancement of the x-ray emission by electron-impurity collisions. The atomic number of the impurity is estimated to be approximately 10 times that of H_2, based on the known pressure of H_2 at the time when the x-ray emission is too high by a factor of 2, the base pressure of the system, and the dependence of the x-ray emission on atomic number. Likely impurities are H_2O, O_2, N_2, and CO_2.

The temperature is shown in Fig. XIII-10 as a function of time in the afterglow. The plasma temperature is observed to rise with time as the plasma is lost from the mirror

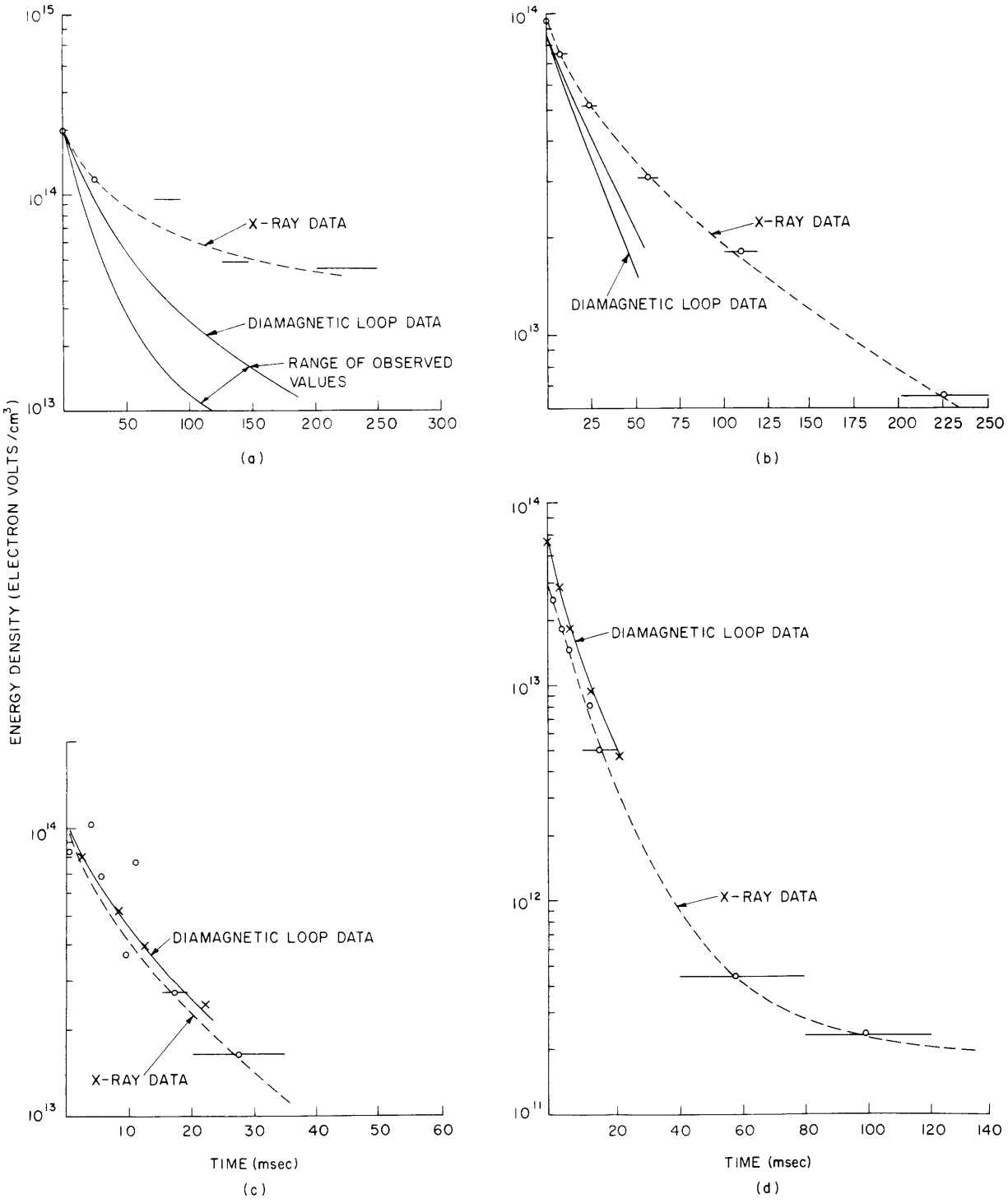

Fig. XIII-9. Plasma energy density decay determined from x-ray spectra and plasma diamagnetism. (a) Normal operation. (b) 2 times normal gas pulse. (c) 5 times normal gas pulse. (d) 10 times normal gas pulse.

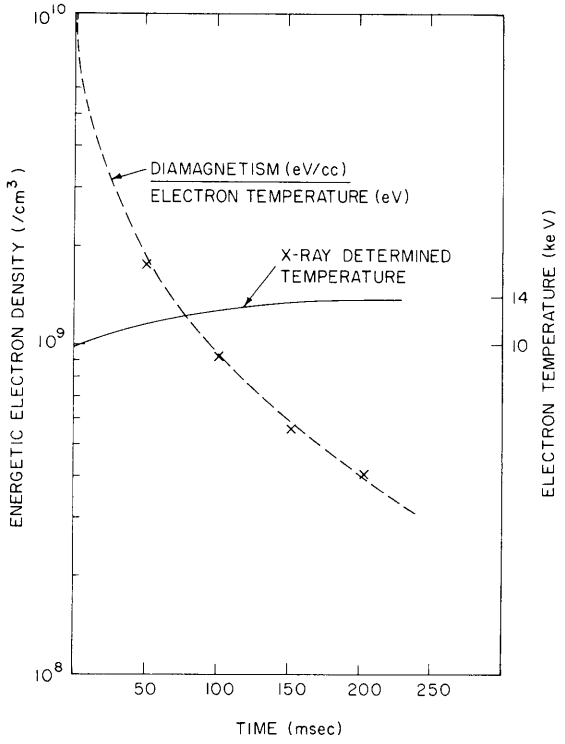

Fig. XIII-10. Temperature and density of the hot component of the plasma.

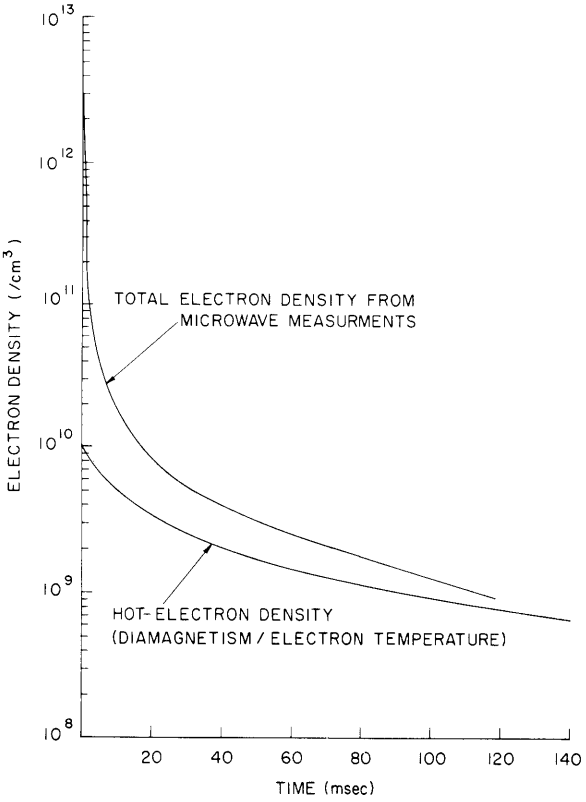

Fig. XIII-11. Decay of total electron density and hot component of electron density.

system. The high-energy electron density is shown in Figs. XIII-10 and XIII-11, as determined by dividing the transverse energy density (diamagnetism) by the mean electron energy determined from the x-ray spectra. Figure XIII-11 illustrates the decays of the total electron density and the hot component of the electron density.

A low-level beam pulser is being used, at present, with the electron gun to excite oscillations in the afterglow following a beam-plasma discharge.

The author wishes to acknowledge the use of the facilities of the National Magnet Laboratory for the experimental work reported here.

R. R. Bartsch

References

1. T. J. Fessenden, "Pulsed Electron-Cyclotron Resonance Discharge," Technical Report 442, Research Laboratory of Electronics, M.I.T., Cambridge, Mass., March 15, 1966.

3. CROSS-FIELD BEAM-PLASMA EXPERIMENTS

The cross-field beam-plasma experiment previously described[1,2] has been operated with a hollow, axially flowing beam and a hollow spiraling beam. These beams have not been pulsed but operated continuously. Observations have been made as these beams passed through a background gas. Various beam densities and gas pressures have been used. The initial observations are presented in this report.

a. Low Gas Pressure, Weak Beam

Low-frequency oscillations have been observed as an axially flowing, hollow beam of approximately 300 volts and 3.5 μpervs passed through a background gas of pressure $1\text{-}5 \times 10^{-7}$ mm Hg. Under these conditions, a plasma was formed by the beam only in the region of the beam particles. These low-frequency oscillations have been observed as a modulation of the collector current and on a radial probe placed near the beam. For a low perveance beam (3 μpervs) these oscillations were essentially pure sine waves in the neighborhood of 100-200 kHz. Their frequency increased when the ion mass was decreased and as the beam density was increased. Increasing the beam density also caused these oscillations to spread in frequency. First harmonics were observed. Then the spectrum spread and became continuous. At a beam perveance of approximately 30 μpervs, the spectra appeared as shown in Fig. XIII-12. This particular perveance

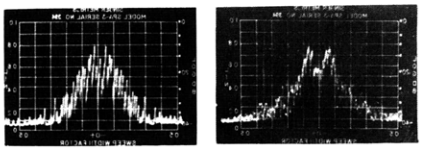

400 kHz PER DIVISION
0 CENTER FREQUENCY

(a)

200 kHz PER DIVISION
0 CENTER FREQUENCY

(b)

Fig. XIII-12.

Low-frequency Spectrum.
(a) 400 kHz per division, center frequency = 0.
(b) 200 kHz per division, center frequency = 0.

(30 μpervs) was also characteristic of beam breakup which is described here.

When a spiraling beam was employed a low-frequency behavior similar to the one described above was observed. The perveances for this beam are also similar to the axially flowing beam if only the axial voltage is used.

b. Low-Pressure, Strong Beam

With a weak (~3.00 μpervs) axially flowing hollow beam, a sharp, well-defined ring of light was formed just in front of the collector (Fig. XIII-13a). Increasing the beam perveance by increasing the beam density caused an increase in the collector current until ~30 μpervs. At this point, the beam current made a drop (Fig. XIII-14) and the pattern

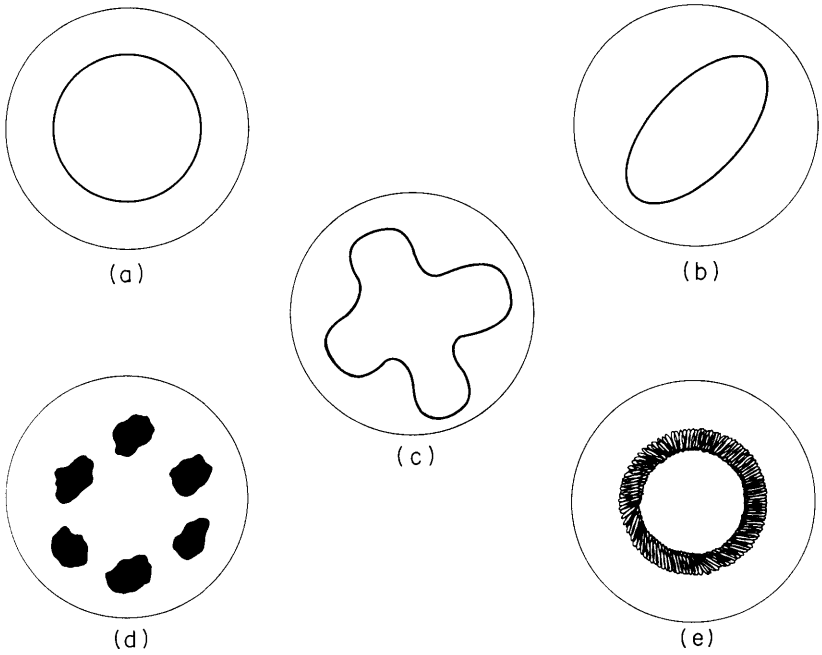

Fig. XIII-13. Beam breakup.

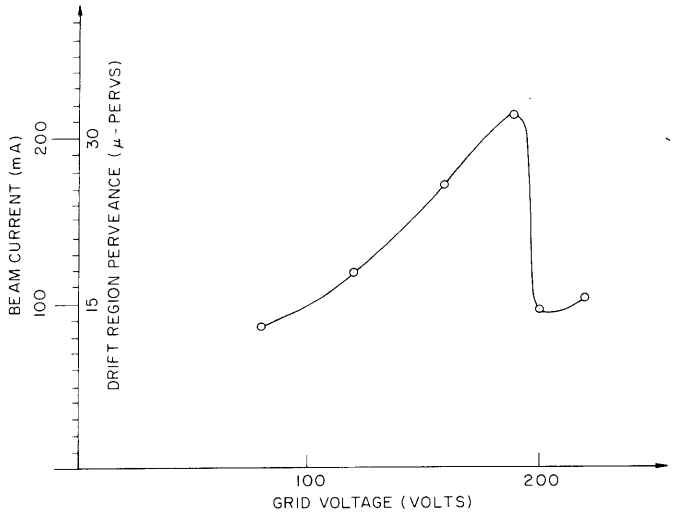

Fig. XIII-14. Beam current vs gun grid voltage at fixed beam voltage.

at the collector takes on one of the shapes shown in Figs. XIII-13b-d. If ℓ is the azimuthal wave number, Fig. XIII-13b is an $\ell = 2$ mode, Fig. XIII-13c, an $\ell = 4$ mode, and Fig. XIII-13d, an $\ell = 6$ mode. An $\ell = 1$ mode would correspond to a shift of the circular pattern in a particular direction, and has not been observed. The different ℓ modes were obtained for different values of magnetic field and beam voltage, and were treated as fixed variables in the experiment.

By using a spiraling beam, the breakup appeared to be different. The beam current also behaved as shown in Fig. XIII-14. For low perveances the spiraling beam hit the collector in a well-defined ring as in Fig. XIII-13a. At the critical perveance (~30 μpervs), however, where the current dropped, the pattern at the collector smeared, as shown in Fig. XIII-13e. With the spiraling beam, no stationary patterns were observed, which occurred for the straight flowing beam.

c. Intermediate Pressure, Weak Beams

Operating the system at a background gas pressure of approximately 3×10^{-5} mm Hg and using a weak beam resulted in oscillations in the neighborhood of the electron-cyclotron frequency. These oscillations were also seen on the collector current and the radial probe. An oscillation first set in at a beam perveance of ~4.35 μpervs at an approximate frequency of 65 mHz. The frequency of this oscillation appeared to have a dependence only on the magnetic field and was linearly proportional. Increasing the beam perveance destroyed this oscillation, until it reached a value of 5 μpervs. At this value, an oscillation set in at approximately 95 mHz. This frequency increased with increasing magnetic field and also with increasing beam density.

These oscillations at and above the electron-cyclotron frequency could be observed on both the spiraling and straight flowing beams.

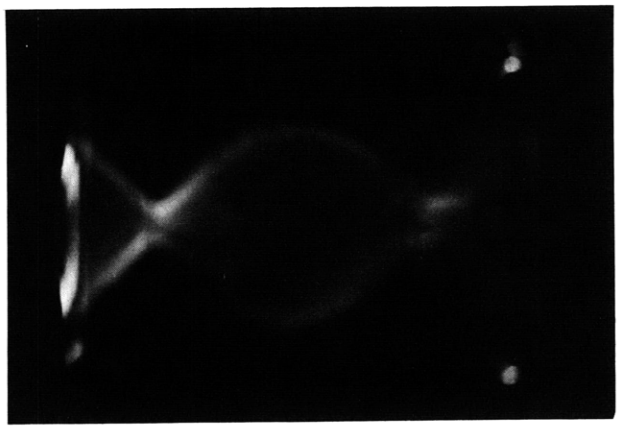

Fig. XIII-15. Beam spiraling through the axis.

At the present time, we continue the investigation of the low-frequency oscillations and the beam breakup.

d. Beam

Our experiments have dealt with a hollow cylindrical beam, either straight-flowing or spiraling. It is possible to create many other types of beams in our experiment.[1] Fig. XIII-15 shows the beam that results when there is no magnetic field in the gun region. The beam particles then spiral synchronously through the axis of symmetry. Here the gun is on the left. The collector and a screen grid are on the right.

B. Kusse

References

1. B. Kusse and A. Bers, "Cross-Field Beam-Plasma Interactions," Quarterly Progress Report No. 82, Research Laboratory of Electronics, M.I.T., July 15, 1966, pp. 154-157.
2. B. Kusse and A. Bers, "Cross-Field Beam-Plasma Experiment," Quarterly Progress Report No. 84, Research Laboratory of Electronics, M.I.T., January 15, 1967, p. 144.

4. EXPERIMENTAL INVESTIGATION OF A BEAM-PLASMA INTERACTION IN A MINIMUM-B FIELD

This experiment is designed to study (a) the hydromagnetic stability properties of a plasma produced in a beam-plasma interaction in an axisymmetric mirror confinement field stabilized by the addition of a hexapole field, and (b) any possible effects of the minimum B field on the beam-plasma interaction.

Charged particles tend to attach themselves to magnetic field lines, by virtue of the conservation of magnetic moment. The radial confinement of the plasma away from the material walls is achieved by means of a static magnetic field. The axial confinement along the field lines is achieved by shaping the uniform static field into an axisymmetric mirror field. The collective behavior of the charged particles in the plasma may give rise, however, to instabilities that destroy the confinement.

The experiment described in this report is being carried out in a slightly modified version of system A. In a series of experiments that were carried out in the same experimental device by H. Y. Hsieh and B. Hartenbaum (in System B), a number of instabilities were observed that led to the eventual loss of confinement of the plasma. We suspect that one of these instabilities is the hydromagnetic interchange instability.

The interchange instability is driven by the negative radial gradient in the magnetic field at the center region of the axisymmetric mirror.[1] The radial gradient of the magnetic field can be reversed in the region of interest by superimposing a multipole cusp magnetic field. A minimum-B magnetic field that is stable against the interchange instability is thus obtained.

a. Experimental Arrangement

A description of the present experimental system can be found in H. Y. Hsieh's doctoral thesis.[2] For this experiment, glass tubing, 3 3/4 in. in diameter and 16 in. long, was installed in system A in the interaction region. This is illustrated in Fig. XIII-16. The magnetic mirror is formed by two coils separated by a distance of ~10.5 in. between their mirror faces, with iron cylinders as magnetic shields placed in front of the electron gun and the collector to produce a field of almost parabolic shape. Magnetic fields in the center region are approximately 400 and 250 Gauss for a current in the coils of 18 and 10 Amps, respectively, with a mirror ratio of approximately 3.

An oxide-coated cathode assembly of a VA-220 gun gives an electron beam of a width approximately 0.2 cm at the center region. The beam flows to a water-cooled copper collector. Neutral gas is admitted continuously into the system through a needle valve.

The minimum-B field is generated by a hexapole configuration. This was accomplished by placing 6 hard-drawn copper strips at intervals of 60° on the periphery of the interaction region inside the glass tubing. The stabilizing field is pulsed during the

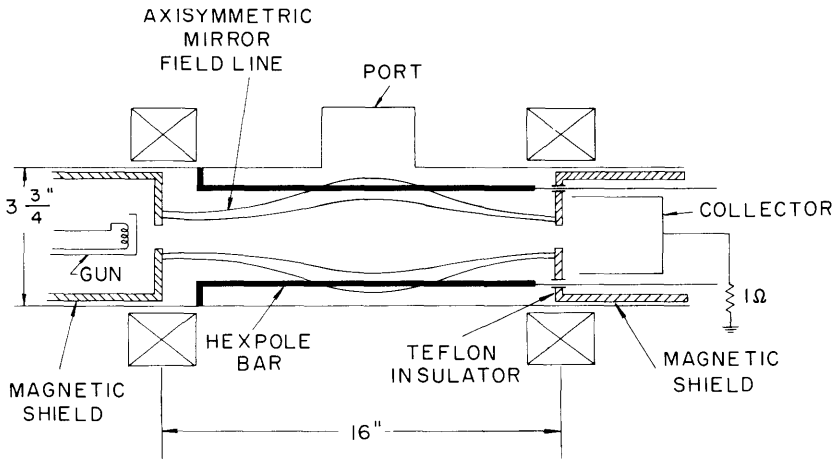

Fig. XIII-16. Experimental apparatus.

discharge at a fixed time, which can be adjusted by a delay circuit connected to the beam pulser.

A simple computation, based on the hexapole's stored magnetic energy in the interaction region, shows that a current pulse with a peak value of 1 kamp is required to generate the stabilizing minimum-B field. Before the discharge, the magnetic energy is stored in electric form in a 60 μFd low-inductance capacitor bank. The current is fed to the bars through the inner conductor of a high-voltage coaxial cable. The bank is fired with an ignitron, with a second ignitron crowbaring the bars some time later when the current in the bars has reached its peak value. Fig. XIII-17 is a diagram of the circuit.

The current through the bars can be monitored with a Rogowski coil. The waveform that is obtained is a damped sinusoid with a period of 120 μsec and a rise time to its peak of 30 μsec. Preliminary measurements show that the resulting currents are

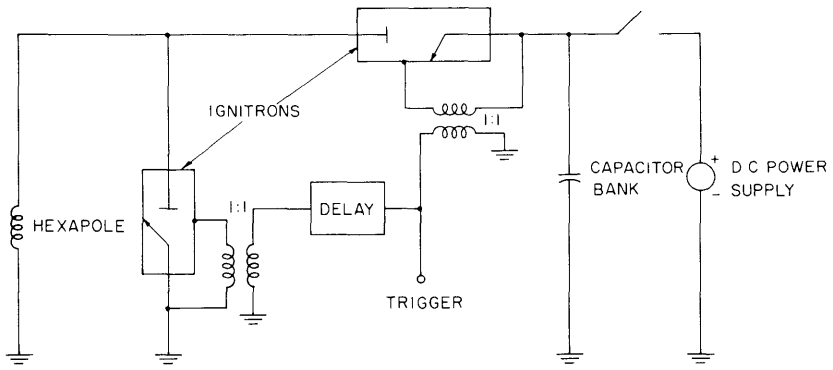

Fig. XIII-17. Hexapole's excitation circuit.

approximately 20% below the theoretical values computed from the stored magnetic energy in the hexapole field.

b. Present Status of Experiment

The experimental arrangement has been built and most of the components tested. In order to study the behavior of the plasma under various experimental conditions, the following diagnostic tools will be used.

(i) RF probe to measure plasma density and to detect plasma oscillations.

(ii) Collector current and, in particular, its time variation that indicates the period of rotation of the unstable plasma.

(iii) Diamagnetic signal to determine the plasma temperature.

c. Combined Minor Multipole Field

Starting from the center of the axisymmetric mirror configuration, the magnetic field increases toward the plane of the mirrors, but decreases radially away from the axis. The multipole field is produced by 2 n rods, placed symmetrically around a cylinder with its axis coincident with that of the axisymmetric mirror field. The multipole field has the property that its magnitude remains constant along a line parallel to the axis and increases radially away from the axis. In order to obtain as uniform a field as possible over the path of the electron beam, we use a hexapole, or higher multipole field, rather than a quadrupole field.

The components of the multipole field[2] are

$$\frac{B_r}{B_\theta} \sim \sum_{k=0}^{\infty} r^{n(2k+1)-1} \frac{\sin n(2k+1)\,\theta}{\cos n(2k+1)\,\theta}$$

Near the axis (small r),

$$|B| \sim r^{n-1}.$$

For a quadrupole, n = 2 and $|B| \sim r$.

For a hexapole, n = 3 and $|B| \sim r^2$.

This shows that variations in |B| around the beam are smaller for the hexapole.

F. N. Herba, J. G. Siambis

References

1. H. Y. Hsieh, "Experimental Study of Beam Plasma Discharge," Ph.D. Thesis, Department of Electrical Engineering, M.I.T., September, 1964.

2. J. Siambis, "Guiding Center Motion of Charged Particles in Combined Mirror-Cusp Magnetic Field," Electronics Research Laboratory, University of California, 1965.

5. ANOMALOUS MILLIMETER MICROWAVE PLASMA DENSITY MEASUREMENTS

We have been concerned with the validity of recent 4-mm interferometric plasma density measurements.[1] Plasma density information is derived from the phase shift observed resulting from the presence of the plasma in a propagation path between two antennas. Such phase-shift measurements are usually interpreted by applying a geometrical optics approximation which, in this application, requires that the size of the plasma be large compared with a wavelength of the probing microwaves.[2] Further, the plasma is usually considered to be a planar slab having sides that are large compared with the size of the probing microwave beam, in order to avoid the difficulty of interpreting the effect of diffraction fields. Hence, the validity of such an interpretation of observed phase shift for small cylindrical plasma columns may be seriously in question.

The interpretation of such microwave phase-shift measurements made recently on the beam-plasma discharge, System C, is subject to difficulties. When this machine is operated with a uniform axial magnetic field, the plasma produced is essentially a long cylinder having a diameter of approximately 2.5 cm. There is some evidence that it is annular in cross section. The plasma, therefore, may be only several wavelengths in thickness and because the microwave beam is of the order of an inch in effective cross section, the validity of the slab approximation is doubtful.

It has been found that an analytic treatment of the relevant propagation problem is impractical within the scope of the present work. Such a problem must accomodate such factors as the finite microwave beam, the near field patterns of the horns, and the presence of a reflective drift tube around the propagation path. An experimental approach was adopted. We shall describe the basic experiment for establishing the validity of the geometrical optics slab approximation.

a. Microwave Propagation Analog

An analog for the microwave propagation, similar to that described by B. B. Rosen,[3] has been built. Since the refractive index of a plasma is less than one, the model for the microwave propagation was constructed by replacing vacuum regions of the path and surrounding geometry with a dielectric ($\kappa = 1.19$) and representing the plasma column by an air-filled hole ($\kappa = 1.0$). The construction is shown in Fig. XIII-18. The dielectric constant ratio corresponds to a plasma density of $0.16\, n_{crit}$, a typical value in System C ($n \approx 10^{13}$ electrons/cc).

Cross section dimensions of beam-plasma discharge System C were scaled smaller by a factor of $\sqrt{\kappa} = 1.09$, thereby preserving the electrical lengths of the actual system. The model measures 10 cm along the dimension parallel to the axis of the cylinder, which represents a length of 26 wavelengths at 70.4 GHz. The steel drift tube of the discharge was modeled by a copper sheet wrapped around the dielectric. Horns and

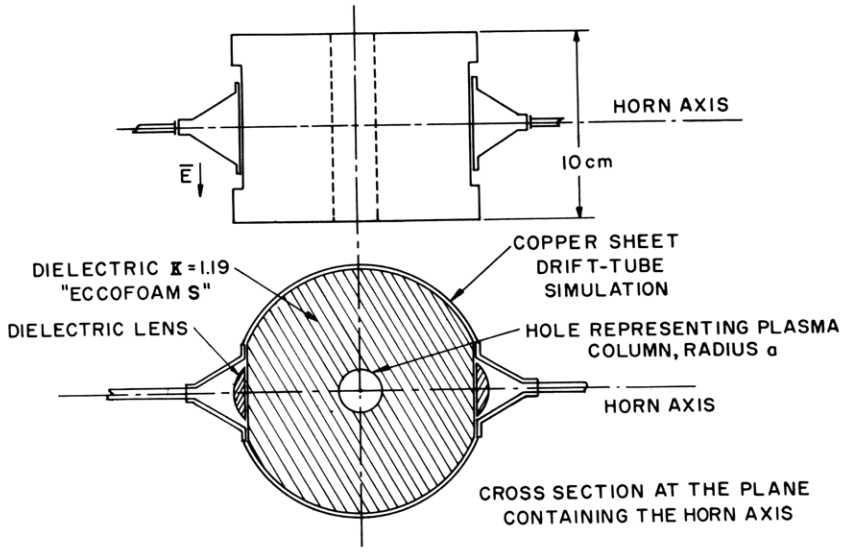

Fig. XIII-18. Microwave propagation analog for scattering from long plasma cylinders.

their lenses were those used in the actual plasma measurements, and were not filled with the dielectric or dimensionally scaled.

The dielectric was "Eccofoam S," a dense, small-celled, polyurethane foam manufactured by Emerson and Cuming, Inc. This material can be shaped by common machining and is available in a variety of dielectric constants with very small loss tangent at millimeter frequencies. Properties of this dielectric at 70.4 GHz were obtained by measuring the amplitude and phase shift of transmission through large slabs, of various thicknesses, using a circuit similar to that shown in Fig. XIII-19.

Amplitude and phase shift caused by the presence of cylindrical holes of various diameters in the model were measured by standard techniques, using phase change

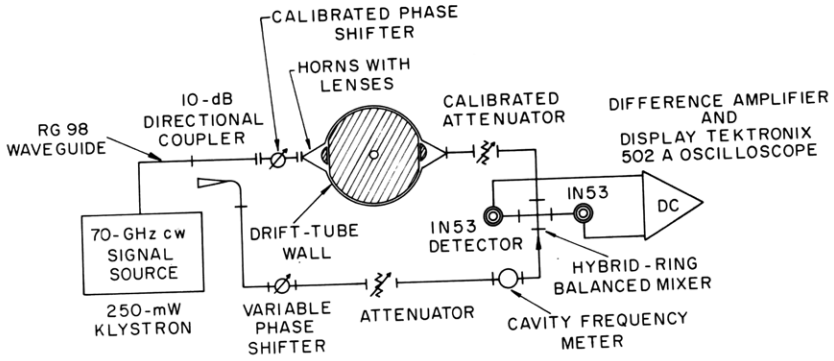

Fig. XIII-19. Microwave bridge circuit.

interferometer circuit of Fig. XIII-19. Polarization was parallel to the cylinder axis. The phase-measuring bridge was adjusted to a null, with a dielectric calibrating cylinder filling the hole. Calibrating cylinders were machined from the same dielectric from which the model was made; hence, their presence represented the "no plasma" condition of zero phase shift and attenuation. We have found that tight dielectric-dielectric interfaces produce no error in this calibration. After calibration and removal of the calibrating cylinder, phase shift was measured by renulling the bridge with a calibrated phase shifter. Similarly, attenuation caused by refraction was measured, by using a precision calibrated attenuator.

b. Results

To examine the geometrical optics, infinite slab approximation phase shift was measured as a function of cylinder radius, a. These data are shown in Fig. XIII-20 compared with the slab approximation for the range of values of interest. Cylinder radii are measured in wavelengths in Eccofoam, $\lambda_E = \lambda_o \kappa^{-1/2} = 3.92$ mm. We have found that the measured phase shift reaches excellent agreement with the slab approximation at a cylinder radius of 2.5 wavelengths, and it is surprisingly close for cylinders as small as 1 wavelength in radius. Note that no phase-shift reversal as observed by Rosen[4] occurs at any point in this range, thereby indicating that the effects of interference of waves around the column is not significant.

Attenuation resulting from refraction for this same range of cylinder sizes is shown in Fig. XIII-21. The large peak occurring at approximately $1.5\ \lambda_E$ is due to the sharp refractive lens effect of the column. This is also in agreement with the experimental work of Rosen.

These results indicate that the slab approximation is applicable to plasmas observed in System C. This appears to be due in part to the good phase correction provided by the horn lenses.

c. Effects of Microwave Beam Misalignment

In an effort to explain an apparent inconsistency of interferometric density measurements on System C the effects of misalignment between the plasma column and the microwave beam were studied. Here, the position of the cylindrical hole representing the plasma was displaced from the center of the model by a distance δ. Phase-shift and attenuation information was obtained for both homogeneous and annular "plasma" cylinders. Annular radial density distributions (hollow-plasma columns) were represented in the model by placing a smaller dielectric cylinder concentrically within a larger hole. Three such annular configurations were considered.

Figure XIII-22 displays the error in phase measurement resulting from column displacement in a direction perpendicular to the horn axis. It appears that displacement

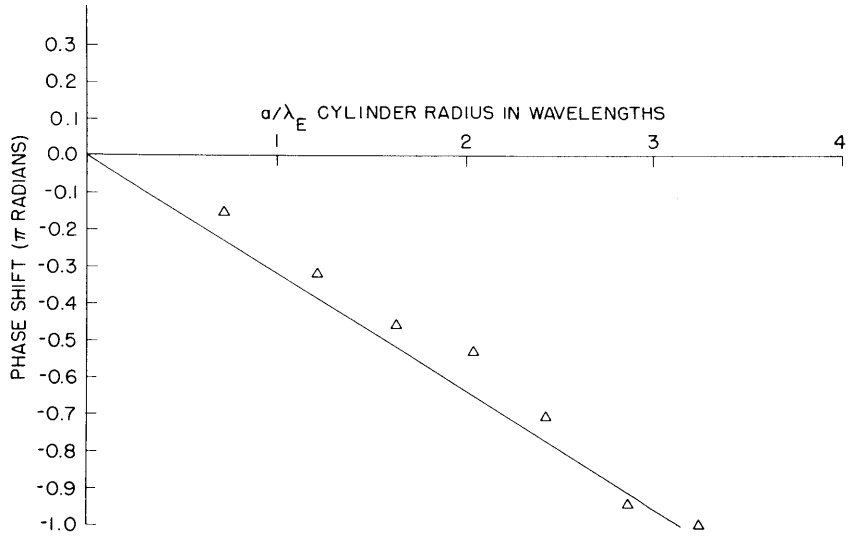

Fig. XIII-20. Measured phase shift vs simulated plasma cylinder radius measured in wavelengths in Eccofoam. Solid Line: geometrical optics slab approximation.

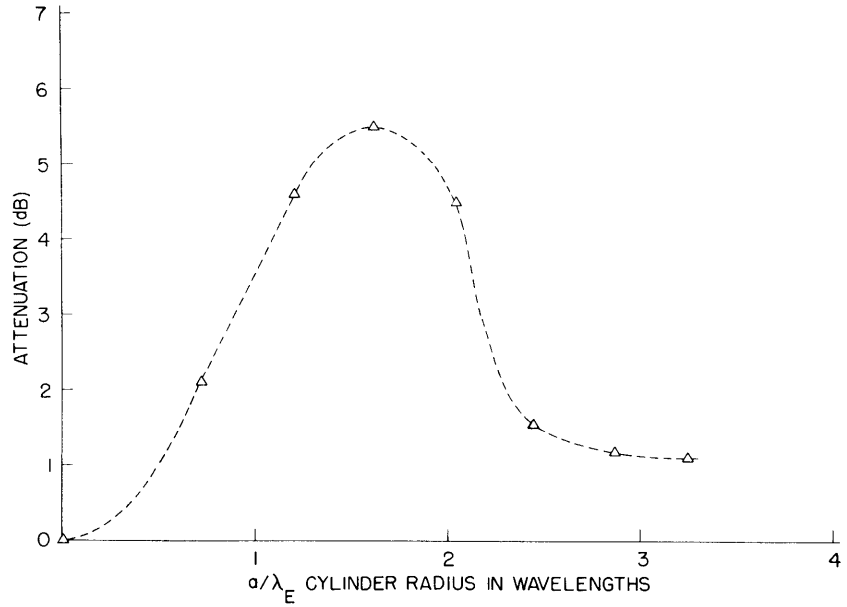

Fig. XIII-21. Measured attenuation vs cylinder radius measured in wavelengths.

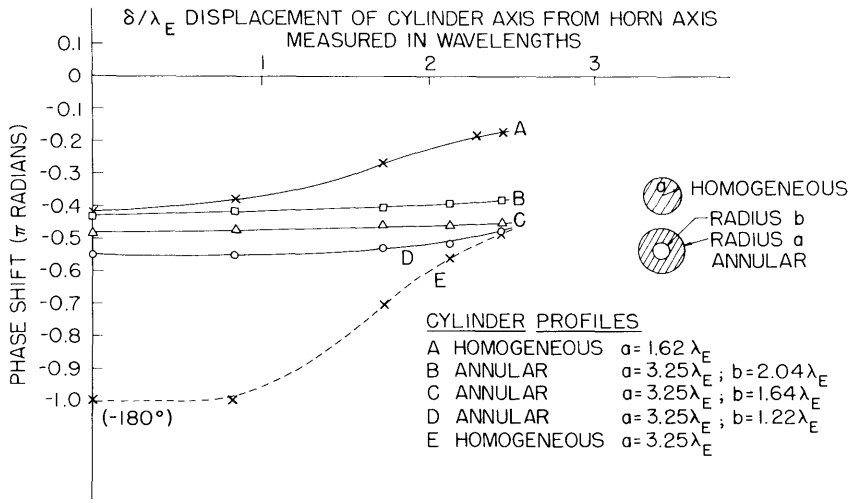

Fig. XIII-22. Measured phase shift vs displacement of simulated plasma cylinder from axis of the horn path.

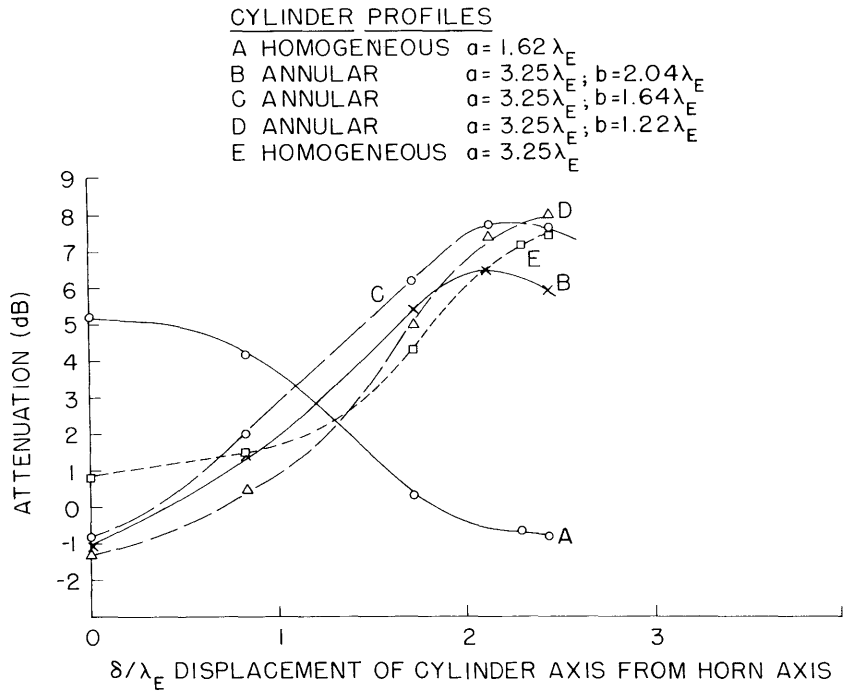

Fig. XIII-23. Measured attenuation vs displacement of cylinder from the axis of the horn path.

from the center of the propagation path in a direction parallel to the horn axis over the range of 3 λ_E does affect observed amplitude or phase shift.

For the same range of displacement, Fig. XIII-23 shows the variation of the attenuation resulting from refraction.

The strong sensitivity of the amplitude or phase to displacement perpendicular to the horn axis for particular sizes and cross sections suggests a possible method for radial-profile diagnosis. For example, a relative insensitivity of the phase-to-horn alignment, together with an amplitude gain through a centered column, would reasonably be interpreted as due to an annular plasma. A technique such as this is of particular value for beam-plasma discharge studies, because of the impracticability of using Langmuir probes within the electron-beam region.

D. M. Perozek

References

1. D. M. Perozek and W. D. Getty, Quarterly Progress Report No. 82, Research Laboratory of Electronics, M. I. T., July 15, 1966, pp. 138-143.
2. M. A. Heald and C. B. Wharton, Plasma Diagnostics with Microwaves (John Wiley and Sons, Inc., New York, 1965), p. 119.
3. B. B. Rosen, The "Inverted Universe" Plasma Analog for Microwaves, Project Matterhorn Technical Memo 85, Princeton University, Princeton, N. J., 1959.
4. Ibid., p. 3.

6. THEORY OF BEAM-PLASMA INTERACTIONS

In studies of small-signal beam-plasma interactions the common approach is to describe both the beam and the plasma by an equivalent dielectric tensor. Such a formulation is convenient for studying interactions with characteristic wavelengths that are short compared with the dimensions of the plasma or beam (which is usually smaller), so that boundary effects are relatively unimportant. When boundary effects become important the dielectric tensor formulation imposes a restrictive description of the particles at the boundary, which may not be consistent with their true dynamics.[2,3] Thus, for example, the surface-charge model for the dynamics at a beam-plasma boundary is of questionable validity. Recent computer experiments on a similar boundary problem indicate that the particle motion is highly nonlaminar.[4]

We shall outline a new approach to describing beam-plasma interactions that should be particularly suited for thin beams and wavelengths large compared with beam thickness. In this development we first study the excitation of the plasma by beam-density perturbations, and then describe the dynamics of the beam perturbations in the average fields over the beam cross section. The thin beam is allowed to have an arbitrary unperturbed density distribution, and moves rigidly. We use the electrostatic approximation throughout.

a. Excitation of Plasma Waves by an External Charge Source

Consider a plasma consisting of s-types of charged carriers and an external charge density distribution ρ_{ext}. In the electrostatic approximation we describe this by

$$\nabla \cdot \epsilon_o \overline{E} - \sum_s e_s n_s = \rho_{ext} \tag{1}$$

$$\overline{E} = -\nabla \Phi \tag{2}$$

and

$$n_s = \int f_s(\overline{r}, \overline{w}, t)\, d^3w$$

$$= F_{s\ op}(\overline{r}, t)\ \Phi, \tag{3}$$

where f_s is the perturbed distribution function for the particles of species s, and Eq. 3 represents the formal solution of the Vlasov equation. For a homogeneous plasma in a magnetic field, and fields with dependence $\exp[-i\omega t + i\overline{k}\cdot\overline{r}]$,

$$F(\omega, \overline{k}) = \frac{k^2 \epsilon_o}{e_s} [1 - K_\ell(\omega, \overline{k})], \tag{4}$$

where

$$K_\ell(\omega, \bar{k}) = \frac{\bar{k} \cdot \bar{\bar{K}}(\omega, \bar{k}) \cdot \bar{k}}{k^2} \tag{5}$$

is the longitudinal dielectric coefficient. Three examples of this follow.

(a) Collisionless plasma with unperturbed distribution function $f_o(w_\perp, w_\parallel)$:

$$K_\ell = 1 + \int d^3w \frac{\omega_p^2}{k^2} \sum_n \frac{J_n^2\left(\frac{k_\perp w_\perp}{\omega_c}\right)\left[\frac{n\omega_c}{w_\perp}\frac{\partial f_o}{\partial w_\perp} + k_\parallel \frac{\partial f_o}{\partial w_\parallel}\right]}{(\omega - k_\parallel w_\parallel - n\omega_c)}. \tag{6}$$

(ii) If f_o is a Maxwellian with $v_T^2 = \kappa T/m$,

$$K_\ell = 1 + \frac{\omega_p^2}{k^2 v_T^2}\left[1 + \sum_n I_n(\lambda)\, e^{-\lambda}\, \xi_o Z(\xi_n)\right], \tag{7}$$

where

$$\lambda = \left(\frac{k_\perp v_T}{\omega_c}\right)^2$$

$$\xi_n = \frac{\omega - n\omega_c}{k_\parallel v_T \sqrt{2}}$$

Z is the plasma dispersion function

I_n is the modified Bessel function.

(iii) For a cold plasma,

$$K_\ell = \frac{1}{k^2}\left[k_\perp^2 K_\perp + k_\parallel^2 K_\parallel\right], \tag{8}$$

where $K_\perp$ and $K_\parallel$ are the usual relative dielectric coefficients of a cold plasma in a magnetic field.

With the external source density ρ_{ext} the problem becomes inhomogeneous, and $F(\omega, \bar{k})$ must be converted to an operator. Formally, we can let $-ik_\perp \rightarrow \partial/\partial x$ and $-ik_\parallel \rightarrow \partial/\partial z$, and obtain

$$\left\{\nabla^2 + \sum_s \left[k^2(1 - K_{s\ell})\right]_{op}\right\} \Phi = -\frac{\rho_{ext}}{\epsilon_o}. \tag{9}$$

b. Electron-Beam Perturbations as a Charge Density Source

The external source in Eq. 9 will now be described in terms of perturbations of a thin electron beam.

$$\rho_{ext} = en, \tag{10}$$

where n is the first-order perturbation in the beam particle density. The unperturbed density of the beam is assumed to be a function of position in the beam cross section

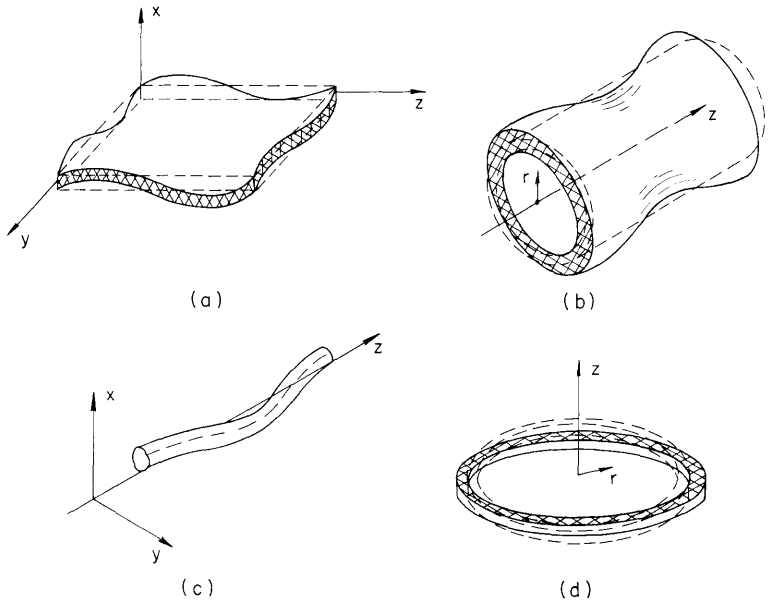

Fig. XIII-24. Examples of thin beams and their perturbations.
(a) Sheet beam, with rigid motion in x.
(b) Hollow beam, with rigid motion in r.
(c) Pencil beam, with rigid motion in x and y.
(d) Ring beam, with rigid motion in r and z.

$n_o(\bar{r}_{cs})$. The beam perturbations are characterized by a displacement vector $\bar{\delta}$ which is rigid in the direction of $\bar{r}_{cs}$. The beam particle density perturbation then is

$$n = -\nabla \cdot (n_o \bar{\delta})$$

$$= -n_o \nabla \cdot \bar{\delta} - \bar{\delta} \cdot \nabla n_o. \tag{11}$$

Four examples follow.

(i) Sheet beam (Fig. XIII-24a).

$$n_o(x)$$

$$\bar{\delta} = \bar{\delta}_o e^{-j\beta_y y} e^{-j\beta_z z}$$

$$n = -n_o(-j\beta_y\delta_y - j\beta_z\delta_z) - \delta_x \frac{\partial n_o}{\partial x}. \tag{12}$$

(ii) Hollow beam (Fig. XIII-24b).

$$n_o(r)$$

$$\bar{\delta} = \bar{\delta}_o e^{-j\beta_z z} e^{-jm\theta}$$

$$n = -n_o(-jm\delta_\theta - j\beta_z\delta_z) - \delta_r \frac{\partial n_o}{\partial r}. \tag{13}$$

(iii) Pencil beam (Fig. XIII-24c).

$$n_o(x, y)$$

$$\bar{\delta} = \bar{\delta}_o e^{-j\beta_z z}$$

$$n = -n_o(-j\beta_z\delta_z) - \delta_x \frac{\partial n_o}{\partial x} - \delta_y \frac{\partial n_o}{\partial y} \tag{14}$$

(iv) Ring beam (Fig. XIII-24d).

$$n_o(r, z)$$

$$\bar{\delta} = \bar{\delta}_o e^{-jm\theta}$$

$$n = -n_o(-jm\delta_\theta) - \delta_r \frac{\partial n_o}{\partial r} - \delta_z \frac{\partial n_o}{\partial z}. \tag{15}$$

c. Beam Dynamics in Fields Averaged over the Beam Cross Section

We define an average over the beam cross section

$$\langle\ \rangle = \frac{1}{A_b} \int_{A_b} da, \tag{16}$$

where A_b is the beam cross section. The equation of motion for the first-order beam displacements then is

$$\frac{d^2}{dt^2}\left\langle mn_o\bar{\delta}\right\rangle = e\left[\left\langle -n_o\nabla\Phi\right\rangle + \left\langle n_o\frac{d\bar{\delta}}{dt}\times\bar{B}_o\right\rangle\right] \tag{17}$$

or, for the nonrelativistic case,

$$\frac{d^2}{dt^2}\bar{\delta} = \frac{e}{m}\left[\frac{\left\langle -n_o\nabla\Phi\right\rangle}{\left\langle n_o\right\rangle} + \frac{d\bar{\delta}}{dt}\times\bar{B}_o\right]. \tag{18}$$

d. Beam-Plasma System

The small-signal dynamics of the beam-plasma system may now be described (in the electrostatic approximation) by Eqs. 9, 10, 11, and 17 or 18. From Eqs. 9, 10, and 11, we can find $\Phi(\bar{\delta})$, which when substituted in Eq. 18 allows one to study the stability of the beam perturbations, δ.

A. Bers

References

1. R. J. Briggs, Electron-Stream Interaction with Plasmas (The M. I. T. Press, Cambridge, Mass., 1964).
2. D. L. Bobroff, H. A. Haus, and J. W. Kluver, J. Appl. Phys. 33, 2934 (1962).
3. W. P. Allis, S. J. Buchsbaum, and A. Bers, Waves in Anisotropic Plasmas (The M. I. T. Press, Cambridge, Mass., 1963).
4. H. M. Schneider, Phys. Fluids 9, 2298 (1966).

7. DISPERSION RELATIONS FOR BEAM-PLASMA INTERACTIONS

We shall present the detailed formulation of some beam-plasma interactions that were outlined in Section XIII-A. 6. We restrict ourselves to a cold-plasma model and consider, first, a pencil beam, and then a thin-sheet beam. In the first case the plasma is assumed to be unbounded, and in the second case the effects of boundaries on the plasma are included.

a. Pencil Beam in an Unbounded Plasma

Consider an electron beam with an unperturbed density distribution $n_o(x, y)$ and velocity $v_o i_z$ immersed in a uniform, infinite, cold plasma. A longitudinal (z-directed) static magnetic field $\vec{B}$ is applied (Fig. XIII-25).

The beam is assumed to be neutralized in its unperturbed state, and the beam density is small compared with the plasma density.

The displacement $\vec{\delta}(z, t)$ of the beam is assumed to be a function of z only, that is, it is independent of position in a given transverse plane. This "rigid-beam" approximation allows for great simplification of the analysis.

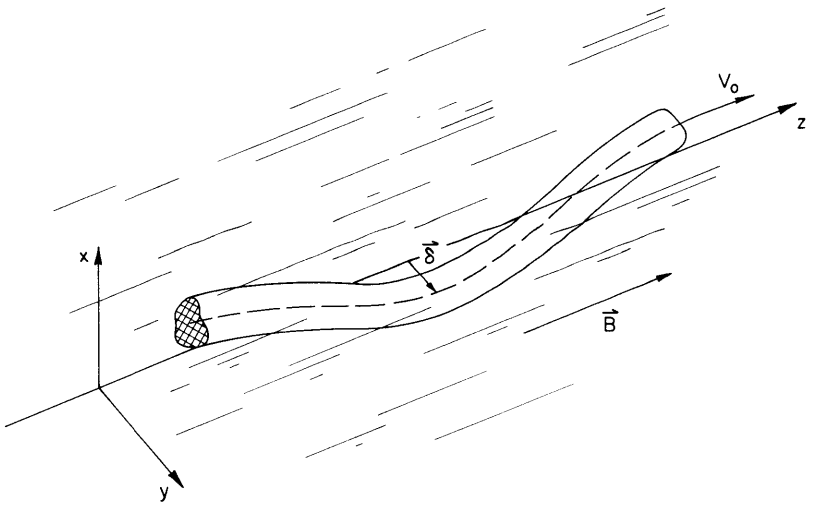

Fig. XIII-25. Pencil beam and its rigid perturbation δ.

For convenience, Cartesian coordinates will be used in the following treatment. This permits Fourier analysis of the beam density and electric potential. If cylindrical coordinates are used, Fourier-Bessel analysis must be employed.

Wave solutions of the form $\exp j(\omega t - \beta z)$ are assumed for the electrostatic potential ϕ, the beam displacement $\vec{\delta}$, and the perturbed beam electron density n_1.

Poisson's equation[1] then reads

$$K_{\perp}\left(\frac{\partial^2}{\partial x^2}+\frac{\partial^2}{\partial y^2}\right)\phi(x,y)-\beta^2 K_{\parallel}\phi(x,y)=\frac{e}{\epsilon_o}\left[\delta_x\frac{\partial n_o}{\partial x}+\delta_y\frac{\partial n_o}{\partial y}+n_o(-j\beta)\,\delta_z\right], \tag{1}$$

where $K_{\perp}$ and $K_{\parallel}$ are components of the dielectric tensor as introduced previously.

The Lorentz equation[2] written out in Cartesian components, gives

$$\begin{aligned}
-\Omega^2\delta_x &= \frac{e}{m}\,\frac{\left\langle -n_o\frac{\partial\phi}{\partial x}\right\rangle}{\langle n_o\rangle}-j\omega_c\Omega\delta_y\\
-\Omega^2\delta_y &= \frac{e}{m}\,\frac{\left\langle -n_o\frac{\partial\phi}{\partial y}\right\rangle}{\langle n_o\rangle}+j\omega_c\Omega\delta_x\\
-\Omega^2\delta_z &= \frac{e}{m}\,\frac{\langle j\beta n_o\phi\rangle}{\langle n_o\rangle},
\end{aligned} \tag{2}$$

where $\omega_c \equiv -\frac{eB}{m}$ is the cyclotron frequency for an electron, and $\Omega \equiv (\omega-\beta v_o)$ is the Doppler-shifted frequency for the moving beam. The quantities in angular brackets are to be averaged over the cross section of the beam. Thus

$$\langle n_o\rangle \equiv \frac{1}{\tau^2}\int_{-\infty}^{\infty}\!\!\int n_o(x,y)\,dxdy, \tag{3}$$

where τ^2 is some suitably defined cross-section beam area; it is introduced merely for normalization purposes.

The beam profile $n_o(x,y)$ and the transverse potential distribution $\phi(x,y)$ can be expressed in terms of their spatial Fourier transforms:

$$\begin{aligned}
n_o(x,y) &= \int_{-\infty}^{\infty}\!\!\int n_o(k_x,k_y)\,e^{-jk_xx-jk_yy}\,\frac{dk_x}{2\pi}\,\frac{dk_y}{2\pi}\\
\phi(x,y) &= \int_{-\infty}^{\infty}\!\!\int \phi(k_x,k_y)\,e^{-jk_xx-jk_yy}\,\frac{dk_x}{2\pi}\,\frac{dk_y}{2\pi}.
\end{aligned} \tag{4}$$

Substituting these in Eq. 1, we obtain

$$\phi(k_x,k_y)=\frac{en_o(k_x,k_y)}{\epsilon_o K_{\perp}}\,\frac{(jk_x\delta_x+jk_y\delta_y+j\beta\delta_z)}{k_x^2+k_y^2+q^2}, \tag{5}$$

where $q^2 = \beta^2 \frac{K_\parallel}{K_\perp}$ is the transverse wave number in the plasma. The averages of products in Eq. 2 can be written

$$\left\langle j\beta n_o \phi \right\rangle \equiv \frac{j\beta}{\tau^2} \int_{-\infty}^{\infty}\int n_o(x,y)\, \phi(x,y)\, dxdy$$

$$= \frac{j\beta}{\tau^2} \int_{-\infty}^{\infty}\int n_o^*(k_x,k_y)\, \phi(k_x,k_y) \frac{dk_x}{2\pi} \frac{dk_y}{2\pi}$$

$$\left\langle -n_o \frac{\partial\phi}{\partial x} \right\rangle = \frac{1}{\tau^2} \int_{-\infty}^{\infty}\int jk_x n_o^*(k_x,k_y)\, \phi(k_x,k_y) \frac{dk_x}{2\pi} \frac{dk_y}{2\pi} \tag{6}$$

$$\left\langle -n_o \frac{\partial\phi}{\partial y} \right\rangle = \frac{1}{\tau^2} \int_{-\infty}^{\infty}\int jk_y n_o^*(k_x,y)\, \phi(k_x,k_y) \frac{dk_x}{2\pi} \frac{dk_y}{2\pi}$$

where the star indicates a complex conjugate.

Substituting (5) in (6), and then in (2), we obtain the following form for the force equations:

$$-\Omega^2 \delta_x = -\frac{1}{K_\perp} \frac{e^2 \langle n_o \rangle}{\epsilon_o m} F_x(q\tau)\, \delta_x - j\omega_c \Omega \delta_y \tag{7a}$$

$$-\Omega^2 \delta_y = -\frac{1}{K_\perp} \frac{e^2 \langle n_o \rangle}{\epsilon_o m} F_y(q\tau)\, \delta_y + j\omega_c \Omega \delta_x \tag{7b}$$

$$-\Omega^2 \delta_z = -\frac{1}{K_\perp} \frac{e^2 \langle n_o \rangle}{\epsilon_o m} (\beta\tau)^2 F_z(q\tau)\, \delta_z, \tag{7c}$$

where F_x, F_y, and F_z are dimensionless quantities defined by

$$F_x(q\tau) = \frac{1}{\langle n_o \rangle^2 \tau^4} \int_{-\infty}^{\infty}\int \frac{(k_x\tau)^2 \left| n_o(k_x,k_y) \right|^2}{(k_x\tau)^2 + (k_y\tau)^2 + (q\tau)^2} \frac{d(k_x\tau)}{2\pi} \frac{d(k_y\tau)}{2\pi}$$

$$F_y(q\tau) = \frac{1}{\langle n_o \rangle^2 \tau^4} \int_{-\infty}^{\infty}\int \frac{(k_y\tau)^2 \left| n_o(k_x,k_y) \right|^2}{(k_x\tau)^2 + (k_y\tau)^2 + (q\tau)^2} \frac{d(k_x\tau)}{2\pi} \frac{d(k_y\tau)}{2\pi} \tag{8}$$

$$F_z(q\tau) = \frac{1}{\langle n_o \rangle^2 \tau^4} \int_{-\infty}^{\infty}\int \frac{\left| n_o(k_x,k_y) \right|^2}{(k_x\tau)^2 + (k_y\tau)^2 + (q\tau)^2} = \frac{d(k_x\tau)}{2\pi} \frac{d(k_y\tau)}{2\pi}.$$

Here, τ can be interpreted as a measure of the thickness of the beam.

Equations 7 show that the transverse displacements of the beam are related to each other, but not to the longitudinal displacement. The reason for this is that the field structure associated with longitudinal displacements, when weighted with the beam density and averaged over the beam, yields no net force in the transverse direction.

A case of frequent interest occurs when $n_o(x,y)$ is symmetric with respect to x and y (this includes the circularly symmetric beam). In this case, Eq. 8 shows that

$$F_x(q\tau) = F_y(q\tau) \equiv F_T(q\tau), \tag{9}$$

where the subscript T is used to indicate association with transverse displacements.

In the case of a one-dimensional Gaussian density variation $n_o(x)$, we have in closed form

$$F_T = \frac{1}{\langle n_o \rangle^2 \tau^2} \int_{-\infty}^{\infty} \frac{(k\tau)^2 \left| n_o(k) \right|^2}{(k\tau)^2 + (q\tau)^2} \frac{d(k\tau)}{2\pi}$$

$$= \frac{-Z'(jq\tau/2)}{2\sqrt{\pi}}$$

$$F_z = \frac{1}{\langle n_o \rangle^2 \tau^2} \int_{-\infty}^{\infty} \frac{\left| n_o(k) \right|^2}{(k\tau)^2 + (q\tau)^2} \frac{d(k\tau)}{2\pi}$$

$$= \frac{-jZ(jq\tau/2)}{2\sqrt{\pi}\ (q\tau)},$$

where Z is the plasma dispersion function, and Z' its derivative.

The force equations (7) now become

$$\left[\Omega^2 - \frac{\langle \omega_{pb}^2 \rangle}{K_\perp} F_T(q\tau) \right] \delta_x = j\omega_c \Omega \delta_y \tag{10a}$$

$$\left[\Omega^2 - \frac{\langle \omega_{pb}^2 \rangle}{K_\perp} F_T(q\tau) \right] \delta_y = -j\omega_c \Omega \delta_x \tag{10b}$$

$$\left[\Omega^2 - \frac{\langle \omega_{pb}^2 \rangle}{K} (\beta\tau)^2 F_z(q\tau) \right] \delta_z = 0, \tag{10c}$$

in which we have defined an average of the square of the beam-plasma frequency:

$$\left\langle \omega_{pb}^2 \right\rangle \equiv \frac{e^2 \langle n_o \rangle}{\epsilon_o m}.$$

Equations 10a and 10b give the dispersion relation for the transverse modes:

$$\left[\Omega^2 - \frac{\left\langle \omega_{pb}^2 \right\rangle}{K_\perp} F_T(q\tau)\right]^2 - \omega_c^2 \Omega^2 = 0. \tag{11}$$

The dispersion relation for the longitudinal modes follows immediately from Eq. 10c:

$$\Omega^2 - \frac{\left\langle \omega_{pb}^2 \right\rangle}{K_\perp} (\beta\tau)^2 F_z(q\tau) = 0. \tag{12}$$

This is readily identified as the dispersion for space-charge beam waves coupled to the plasma (through $K_\perp$ and $F_z(q\tau)$).

The transverse waves are more easily interpreted if the roots to Eq. 11 are expressed in the form

$$\Omega_1 \equiv (\omega - \beta v_o)_1 = -\frac{\omega_c}{2} - \left[\left(\frac{\omega_c^2}{2}\right) + \frac{\left\langle \omega_{pb}^2 \right\rangle}{K_\perp} F_T(q\tau)\right]^{1/2}$$

$$\Omega_2 \equiv (\omega - \beta v_o)_2 = \frac{\omega_c}{2} - \left[\left(\frac{\omega_c^2}{2}\right) + \frac{\left\langle \omega_{pb}^2 \right\rangle}{K_\perp} F_T(q\tau)\right]^{1/2}$$

$$\Omega_3 \equiv (\omega - \beta v_o)_3 = -\frac{\omega_c}{2} + \left[\left(\frac{\omega_c^2}{2}\right) + \frac{\left\langle \omega_{pb}^2 \right\rangle}{K_\perp} F_T(q\tau)\right]^{1/2} \tag{13}$$

$$\Omega_4 \equiv (\omega - \beta v_o)_4 = \frac{\omega_c}{2} + \left[\left(\frac{\omega_c^2}{2}\right) + \frac{\left\langle \omega_{pb}^2 \right\rangle}{K_\perp} F_T(q\tau)\right]^{1/2}.$$

In the absence of the plasma ($K_\perp = 1$, $K_{\parallel} = 1$), and for a very thin beam ($q\tau \approx 0$; $F(q\tau) \approx F(0)$), Eq. 13 describes the well-known waves on a filamentary beam (Fig. XIII-26).

The transverse waves are circularly polarized, as can be seen by substituting the roots (13) in the force equation (10) to obtain

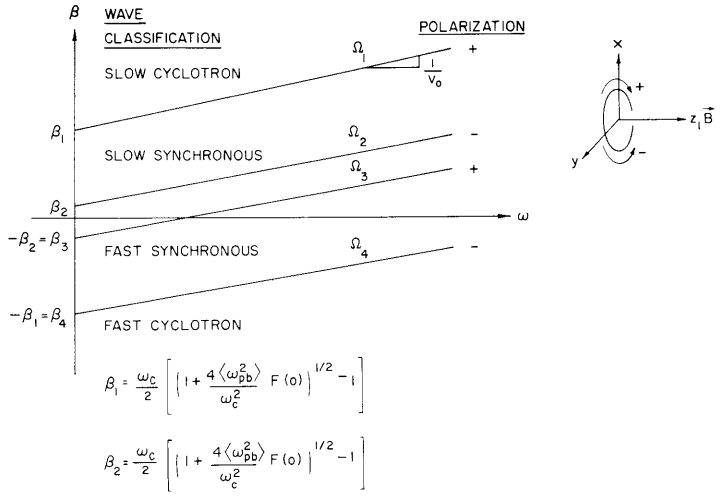

Fig. XIII-26. Waves on a filament – any beam in the absence of a plasma.

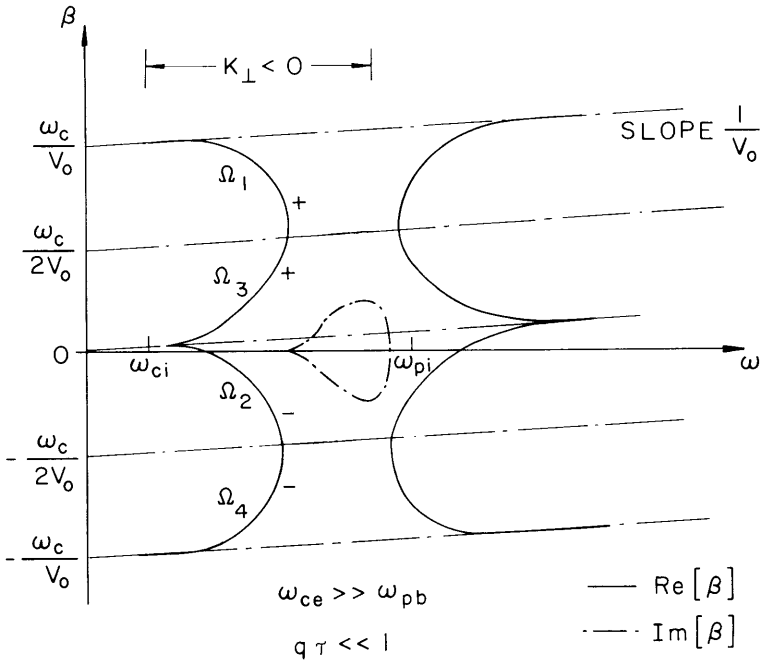

Fig. XIII-27. Low-frequency beam-plasma interactions for a filamentary beam.

$$\frac{\delta_x}{\delta_y} = \begin{cases} -j & (\Omega = \Omega_1, \Omega_3) \\ +j & (\Omega \quad \Omega_2, \Omega_4) \end{cases}. \tag{14}$$

It may be shown that roots Ω_1 and Ω_3 represent waves rotating in the sense of ions in the magnetic field (+ polarization). The other two waves rotate in the opposite sense (− polarization).

As an example of unstable modes that can arise when the plasma is present, Fig. XIII-27 illustrates reactive medium amplification, which arises when $K_\perp$ is negative.

Note, at the onset of amplification, that the waves of similar polarization merge and have the same phase velocities.

b. Sheet Beam in a Bounded Cold Plasma

Finally, consider a sheet beam, infinite and uniform in the y direction, traveling with velocity $v_o \bar{i}_z$ through a cold plasma bounded by two perfectly conducting plates (Fig. XIII-28). A longitudinal magnetic field $B\underline{i}_z$ is applied to the system.

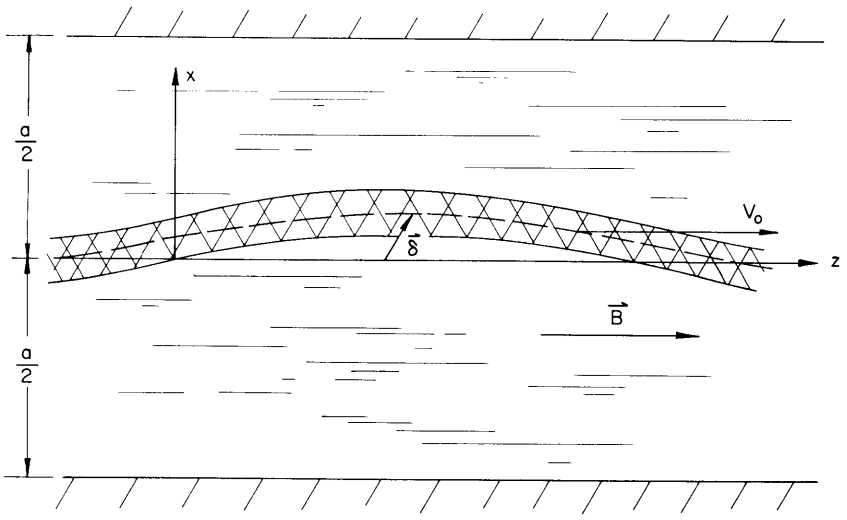

Fig. XIII-28. Sheet beam, and its rigid perturbation δ, in a bounded plasma.

The unperturbed beam is neutralized, with a symmetric density profile $n_o(x)$. The beam displacement $\bar{\delta}$ is independent of both x and y.

If we assume wave solutions of the form $\exp[j(\omega t - \beta z)]$ for the electrostatic potential $\bar{\delta}$, the perturbed density n_1, and the displacement ϕ, Poisson's equation yields

$$\frac{\partial^2\phi(x)}{\partial x^2} + p^2\phi(x) = \frac{e}{\epsilon_o K_\perp}\left[\delta_x \frac{\partial n_o}{\partial x} - j\beta n_o \delta_z\right], \tag{15}$$

where

$$p^2 \equiv -\beta^2 \frac{K_\parallel}{K_\perp}$$

is the transverse wave number in the plasma. The force equations are

$$-\Omega^2\delta_x = \frac{e}{m}\frac{\left\langle -n_o \frac{\partial\phi}{\partial x}\right\rangle}{\langle n_o\rangle} - j\omega_c\Omega\delta_y \tag{16a}$$

$$-\Omega^2\delta_y = j\omega_c\Omega\delta_x \tag{16b}$$

$$-\Omega^2\delta_z = \frac{e}{m}\frac{\langle j\beta n_o\phi\rangle}{\langle n_o\rangle}, \tag{16c}$$

where the quantities in angular brackets are to be averaged over the transverse dimensions of the plasma.

$$\langle n_o\rangle = \frac{1}{a}\int_{-a/2}^{a/2} n_o(x)\,dx. \tag{17}$$

The procedure now is to expand $\phi(x)$ in terms of the eigenfunctions of Laplace's equation, obtained from Eq. 1 by setting the right hand side to zero. These eigenfunctions $\phi_m(x)$ are simply the natural plasma modes in the absence of the beam. Let

$$\phi(x) = \sum_{m=0}^{\infty} A_m\phi_m(x). \tag{18}$$

The eigenfunctions (natural modes) are

$$\phi_m(x) = \begin{cases} \cos\dfrac{m\pi z}{a} & m = 1,3,5\ldots \\ \sin\dfrac{m\pi x}{a} & m = 2,4,6\ldots \end{cases} \tag{19}$$

and the corresponding wave numbers are

$$p_m = \frac{m\pi}{a}. \tag{20}$$

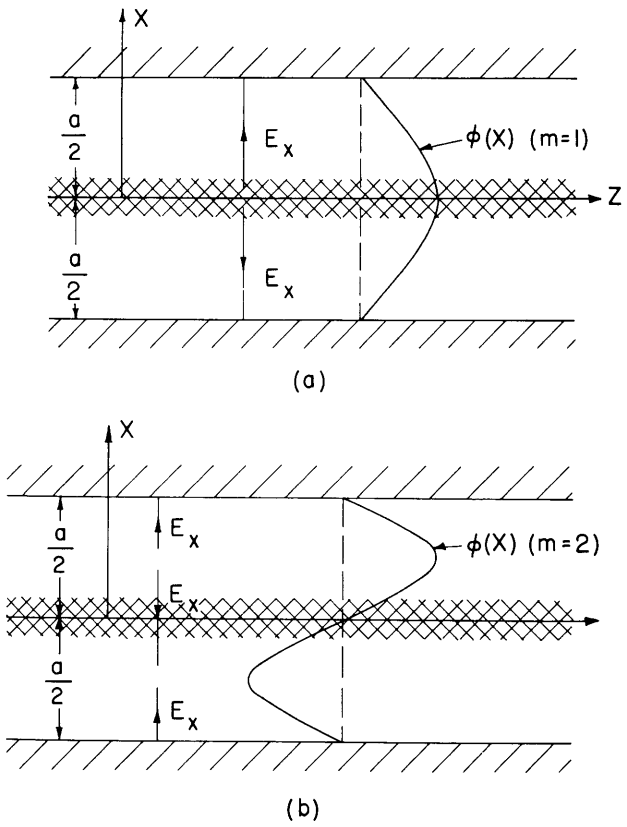

Fig. XIII-29. Field distributions for a sheet beam in a bounded plasma.
(a) Transverse fields for longitudinal displacements.
(b) Transverse fields for transverse displacements.

The two lowest natural modes and associated fields are shown in Fig. XIII-29. Equation 18 can now be written

$$\phi(x) = \sum_{m\ \text{odd}} A_m \cos\frac{m\pi x}{a} + \sum_{m\ \text{even}} A_m \sin\frac{m\pi x}{a}. \tag{21}$$

Substituting Eq. 21 in Eq. 15 and evaluating coefficients A_m, we obtain

$$\phi(x) = -\frac{2e}{\epsilon_o K_\perp}\left\{\sum_{m\ \text{odd}} \frac{j\beta n_m \delta_z}{p^2 - \left(\frac{m\pi}{a}\right)^2}\cos\left(\frac{m\pi x}{a}\right) + \sum_{m\ \text{even}} \frac{\left(\frac{m\pi}{a}\right) n_m \delta_x}{p^2 - \left(\frac{m\pi}{a}\right)^2}\sin\left(\frac{m\pi x}{a}\right)\right\}, \tag{22}$$

where

$$n_m = \frac{1}{a}\int_{-a/2}^{a/2} n_o(x)\cos\frac{m\pi x}{a}\,dx.$$

It can be seen that longitudinal displacements excite only symmetric fields and transverse displacements only antisymmetric fields. This is obvious because of the beam symmetry. Substitution of Eq. 12 in Eq. 16 results in the following form for the force equations:

$$\left\{\Omega^2 + \frac{1}{K_\perp}\frac{e^2\langle n_o\rangle}{m\epsilon_o}\left[\sum_{m\ \text{even}} \frac{2\left(\frac{m\pi}{a}\right)^2}{p^2 - \left(\frac{m\pi}{a}\right)^2}\frac{n_m^2}{\langle n_o\rangle^2}\right]\right\}\delta_x = j\omega_c\Omega\delta_y \tag{23a}$$

$$\Omega^2\delta_y = -j\omega_c\Omega\delta_y \tag{23b}$$

$$\left\{\Omega^2 + \frac{1}{K_\perp}(\beta\tau)^2\frac{e^2\langle n_o\rangle}{m\epsilon_o}\left[\sum_{m\ \text{odd}} \frac{2\frac{n_m^2}{\langle n_o\rangle^2}}{\tau^2\left[p^2 - \left(\frac{m\pi}{a}\right)^2\right]}\right]\right\}\delta_z = 0, \tag{23c}$$

where τ is a characteristic beam thickness introduced for normalization purposes.

Notice in Eq. 23 that the transverse displacements are again uncoupled from the longitudinal displacements. The physical reason for this should be clear from Fig. XIII-29. Longitudinal displacements excite symmetric fields, which when averaged over the beam give no net transverse force. Similarly, transverse displacements do not give rise to a net longitudinal force.

The dispersion relation for the transverse modes is derived from Eqs. 23a and 23b.

$$\Omega^2\left\{\Omega^2 - \omega_c^2 + \frac{1}{K_\perp}\frac{e^2\ n_o}{m\epsilon_o}\left[\sum_{m\ \text{even}} \frac{2\left(\frac{m\pi}{a}\right)^2}{p^2 - \left(\frac{m\pi}{a}\right)^2}\frac{n_m^2}{\langle n_o\rangle^2}\right]\right\} = 0. \tag{24}$$

The double root, $\Omega^2 = 0$, has no physical significance and corresponds to arbitrary displacements in the y direction. The other two roots give cyclotron-type waves.

For longitudinal modes, the dispersion equation is simply given by Eq. 23c.

The stability of this and other dispersion relations pertinent to our experiments are under study at present.

S-L. Chou, A. Bers

References

1. See Eq. 9 in Section XIII-A. 6.
2. See Eq. 18 in Section XIII-A. 6.

8. SHEET MODELS OF THE BEAM-PLASMA DISCHARGE

We have continued the study of the beam-plasma discharge, using superparticles to represent the beam, and the fluid equations to represent the plasma. We are now studying the effects of finite beam diameter on the interaction, by representing the beam with disks. An analytic, linear, finite-diameter beam theory is presented here, for later comparison with computer experiments. The electrostatic approximation will be used throughout (H = 0).

We assume: (i) no transverse beam motion; (ii) plasma transverse motion is unhindered; (iii) no radial variation in v_{bz}; (iv) a cold infinite plasma with a linear density gradient along the beam; and (v) a uniform beam of radius b.

To evaluate assumptions (i) and (ii), we see, from Allis, Buchsbaum, and Bers,[1]

$$v = \frac{e}{m} \begin{matrix} \dfrac{\omega_{1,2}}{j\left(\omega_{1,2}^2 - \omega_c^2\right)} & \dfrac{-\omega_c}{\omega_{1,2}^2 - \omega_c^2} & 0 \\ \dfrac{\omega_c}{\omega_{1,2}^2 - \omega_c^2} & \dfrac{\omega_{1,2}}{j\left(\omega_{1,2}^2 - \omega_c^2\right)} & 0 \\ 0 & 0 & \dfrac{1}{j\omega_{1,2}} \end{matrix} \begin{matrix} E_x \\ E_y \\ E_z \end{matrix} \qquad (1)$$

where

$$\omega_c = \frac{eB_o}{m}$$

$\omega_1 = \omega - kv_o$ for beam electrons

$\omega_2 = \omega$ for plasma electrons.

In System A,

$\omega \approx \omega_p = 2\pi \times 1.5 \times 10^{10}$ Hz

$\omega_c = 2\pi \times 2.8 \times 10^6$ Hz/Gauss

$0 < B_o < 700$ Gauss.

Since $\omega_2 \approx \omega_p^2 \gg \omega_c^2$, assumption (ii) is valid. Assumption (i) requires $\omega_1^2 \ll \omega_c^2$ if the transverse fields are of the same magnitude as the longitudinal field. But

$\omega_1^2 = (\omega - \text{Re } kv_o - j\text{Im } kv_o)^2 \approx -(\text{Im } kv_o)^2 \approx -\left(\frac{\omega_p}{5}\right)^2$, which we obtain by anticipating the results of Fig. XIII-30. Hence the transverse beam motion would be reduced by less

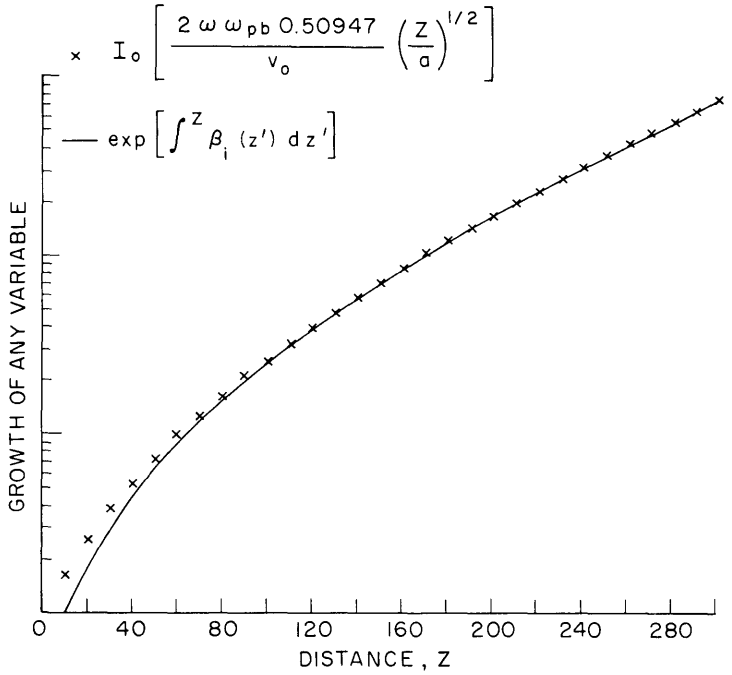

Fig. XIII-30. W K B approximation to the growth of any variable in a finite-diameter beam-plasma interaction, with a linear plasma density gradient. This is compared with the growth of the first-order beam velocity in a one-dimensional beam. Distances normalized to $0.4\, v_{ob}\omega_{po}^{-1}$.

than a factor of 2. For a symmetric mode, however, the transverse field on the axis is zero, and might be expected to be small over the beam. The quantitative effects of assumptions (i) and (iii) are not completely understood.

We assume a cold plasma with a linear density gradient given by

$$\omega_p^2 = \omega^2 + az. \tag{2}$$

For quasi-statics, the pertinent equations are

$$\nabla \cdot (\bar{\bar{K}}_{\parallel} \cdot \nabla\phi) = -\frac{en_b}{\epsilon_o} \tag{3}$$

$$K_{\parallel} = \bar{\bar{I}}\left(1 - \frac{\omega_p^2(z)}{\omega^2}\right) = -\frac{az}{\omega^2}\bar{\bar{I}}. \tag{4}$$

We make Fourier-Bessel transforms in the transverse direction.

$$\Phi_r = \frac{1}{(2\pi)^2} \int_0^\infty dk \int_0^{2\pi} d\phi \, k \, e^{ikr\cos(\theta-\phi)} \, \Phi_k,$$

under the assumption of θ - symmetric modes, or

$$\Phi_r = \frac{1}{2\pi} \int_0^\infty dk \, J_o(k\,r) \, \Phi_k, \tag{5}$$

and

$$\Phi_k = 2\pi \int_0^\infty dr \, r \, J_o(k\,r) \, \Phi_r, \tag{6}$$

Equation 3 becomes

$$\frac{az}{\omega^2} k^2 \, \Phi_k - \frac{a}{\omega^2} \frac{\partial \Phi_k}{\partial z} - \frac{az}{\omega^2} \frac{\partial^2 \Phi_k}{\partial z^2} = - \frac{e n_{bk}}{\epsilon_o}. \tag{7}$$

The conservation equation can be written

$$n_b = -\nabla \cdot [n_{ob}(r) \, \bar{\delta}]$$

or, by using assumption (i),

$$n_{bk} = -n_{ok} \frac{\partial \delta_z}{\partial z}, \tag{8}$$

where δ is the displacement from equilibrium. We use assumption (iii) in the force equation, so that

$$\left[j\omega + v_o \frac{\partial}{\partial z} \right]^2 \quad n_{ob} \quad \delta_z = \frac{e}{m} \left\langle n_{ob} \frac{\partial \Phi}{\partial z} \right\rangle. \tag{9}$$

We define the average as

$$\langle \, \rangle \equiv \lim_{r_o \to \infty} \frac{2\pi}{\pi r_o^2} \int_0^{r_o} dr \, r. \tag{10}$$

Hence

$$\left\langle n_o \Phi \right\rangle = \lim_{r_o \to \infty} \frac{2\pi}{\pi r_o^2} \int_0^{r_o} dr \, r \int_0^\infty \frac{dk}{2\pi} \, k \, n_{ok} \, J_o(k\,r) \int_0^\infty \frac{dk'}{2\pi} \, k' \, \Phi_{k'} \, J_o(k'\,r)$$

or

$$\langle n_o \Phi \rangle = \frac{1}{\pi r_o^2} \int_0^\infty \frac{dk}{2\pi} k\, n_{ok}\, \Phi_k. \tag{11}$$

To proceed further, we use the W K B approximation $\left(\frac{\partial}{\partial z} = -j\beta\right)$. We combine Eqs. 7, 8, 9, and 11 to obtain

$$(\omega - \beta v_o)^2 \frac{-e^2 \beta^2 \omega^2}{m\epsilon_o \langle n_o \rangle \pi r_o^2 a 2\pi} \int_0^\infty \frac{dk\, k\, n_{ok}^2}{[z(\beta^2 + k^2) + j\beta]}, \tag{12}$$

since

$$\begin{aligned} n_o(r) &= n_o \qquad r \leq b \\ &= 0 \qquad r > b \end{aligned} \tag{13}$$

$$n_{ok} = \frac{2\pi n_o b J_1(k b)}{k}. \tag{14}$$

We know that

$$\langle n_o \rangle \pi r_o^2 = \pi b^2 n_o, \tag{15}$$

and hence we define

$$\omega_{pb}^2 = \frac{e^2 n_o}{m\epsilon_o}. \tag{16}$$

Then

$$(\omega - \beta v_o)^2 = \frac{-\omega_{pb}^2 \beta^2 \omega^2 2}{a} \int_0^\infty \frac{dk\, J_1^2(k b)}{k[z(\beta^2 + k^2) + j\beta]} \tag{17}$$

or

$$(\omega - \beta v_o)^2 = \frac{-\omega_{pb}^2 \beta^2 \omega^2}{az(\beta^2 + j\beta/z)} \left[1 - 2I_1\left(b\sqrt{\beta^2 + j\beta/z}\right) K_1\left(b\sqrt{\beta^2 + j\beta/z}\right)\right] \tag{18}$$

If the plasma were homogeneous, we would replace az with $\omega_p^2 - \omega^2$, and drop the $j\beta/z$ terms, which arose from the fact that $\frac{\partial \omega_p^2}{\partial z} \neq 0$. Then Eq. 19 becomes

$$1 - \frac{\omega_p^2}{\omega^2} - \frac{\omega_{pb}^2}{(\omega - \beta v_o)^2} [1 - 2I_1(\beta b)\, K_1(\beta b)] = 0. \tag{19}$$

This can be contrasted with the calculations done under the assumption of transverse beam motion.[2]

$$1 - \frac{\omega_p^2}{\omega^2} - \frac{\omega_{pb}^2}{(\omega - \beta v_o)^2}\, \beta b\, I_1(\beta b)\, K_o(\beta b) = 0. \tag{20}$$

Equations 19 and 20 have different limits as $b \to \infty$. Equation 19 goes to the correct one-dimensional limit, but Eq. 20 becomes

$$1 - \frac{\omega_p^2}{\omega^2} - \frac{\omega_{pb}^2/2}{(\omega - \beta v_o)^2} = 0. \tag{21}$$

Crawford[3] has concluded that the fields of Eq. 20 are due entirely to surface charge at the beam edge, whereas in the one-dimensional limit the fields are due to volume charge. The fields of Eq. 19 are due entirely to volume charge, so that correct limit as $b \to \infty$ is physically reasonable.

We have solved Eq. 18 on the computer, using normalized beam and plasma parameters as given in a previous report,[4] corresponding to typical values in System A.

$$(\omega_{pb}) = 0.1 \qquad \omega = (0.15)^{1/2}$$

$$a = 0.001 \qquad (v_o) = 2.5$$

$$b_n = 4.69.$$

Distances are normalized to $0.4\, v_o/\omega_{po}$, times to ω_{po}^{-1}. ω_{po} corresponds to the peak density in System A.

In the WKB approximation, all first-order plasma and beam parameters grow at the same rate. This growth is shown in Fig. XIII-30. It is compared with $I_o\left[\frac{2\omega\omega_{pb}'}{v_o}\left(\frac{z}{a}\right)^{1/2}\right]$, the growth of the first-order beam velocity in one dimension. The two curves have been matched at $z = 250$ and $z = 300$. We found that $\omega_{pb}' = 0.50947\, \omega_{pb}$ for a match, or an effective beam density reduction factor of approximately 0.25.

J. A. Davis

References

1. W. P. Allis, S. Buchsbaum, and A. Bers, Waves in Anistropic Plasmas (The M.I.T. Press, Cambridge, Mass., 1963), p. 19.

2. E.E. Abraham and F.W. Crawford, "Comparison of Experimental and Theoretical Results of the Beam-Plasma Interaction," Stanford University SU-IPR Report No. 24, August 1965.

3. F. W. Crawford, J. Electronics and Control 19, 217 (1965).

4. J.A. Davis, Quarterly Progress Report No. 84, Research Laboratory of Electronics, M.I.T., January 15, 1967, pp. 145-148.

9. EFFECT OF ESSENTIAL SINGULARITIES ON STABILITY CRITERIA

The interaction of a monoenergetic beam with a cold collisionless plasma, as described by the dispersion relation

$$\frac{\omega_{pb}^2}{(\omega - kv_o)^2} + \frac{\omega_p^2}{\omega^2} = 1, \tag{1}$$

is often cited as a classical example of a convective instability.[1] The purpose of this note is to point out that this is not strictly correct, and to show why caution should be exercised in other examples in which the dispersion relation has roots $k(\omega)$ for which $k \to \infty$ at some real ω. (That is, cases for which there are essential singularities of $F(\omega, z)$ on the real ω axis.[2])

The response $\psi(z, t)$, which is due to an excitation at the plane $z = 0$, has the form

$$\psi(z, t) = \int_{-\infty - j\sigma}^{\infty - j\sigma} \int_{-\infty}^{+\infty} \frac{e^{j(\omega t - kz)}\, s(\omega)}{\left(k - \frac{\omega}{v_o} - K(\omega)\right)\left(k - \frac{\omega}{v_o} + K(\omega)\right)} \frac{dk d\omega}{(2\pi)^2}, \tag{2}$$

where

$$K(\omega) = \frac{\omega_{pb}}{v_o}\left(1 - \omega_p^2/\omega^2\right)^{-1/2}. \tag{3}$$

The source considered here is of the form $s(t, z) = \delta(z) \exp(j\omega_o t)$ for $t > 0$, for which $s(\omega) \sim (\omega - \omega_o)^{-1}$. The k integration can be readily done, and yields

$$\psi(z, t) = -\int_{-\infty - j\sigma}^{+\infty - j\sigma} s(\omega)\, e^{j\omega(t - z/v_o)} \frac{\sin K(\omega)\, z}{K(\omega)} \frac{d\omega}{2\pi} \tag{4}$$

for $z > 0$. The integrand in Eq. 4 has an essential singularity at $\omega = \omega_p$ in addition to the simple pole at $\omega = \omega_o$, and this fact complicates its asymptotic evaluation. We shall consider both t and z to be farily large, and evaluate the integral asymptotically by a saddle-point method. Let $\tau = t - z/v_o$ and

$$\phi(\omega) \equiv \omega\tau - K(\omega)z. \tag{5}$$

The saddle points are determined by $\partial\phi(\omega)/\partial\omega = 0$. For $\omega_p\tau \gg k_b z$ (where $k_b \equiv \omega_{pb}/v_o$), there is a saddle point at

$$\omega_s = \omega_p\left[1 + \frac{1}{2}\left(\frac{k_b z}{\omega_p \tau}\right)^{2/3} e^{-j2\pi/3}\right] \tag{6}$$

for which

$$\phi(\omega_s) = \omega_p\tau + \frac{3}{2}(k_b z)^{2/3}(\omega_p\tau)^{1/3} e^{-j2\pi/3}. \tag{7}$$

The saddle-point integration leads to the asymptotic response

$$\psi(z,t) \sim \exp\left\{j\omega_p\tau + \frac{3\sqrt{3}}{4}(k_b z)^{2/3}(\omega_p\tau)^{1/3}\right\} \tag{8}$$

for $z > 0$ ($\psi = 0$ for $z < 0$), independent of the source frequency ω_o. The intuitive reason why this model predicts continued growth in time, and not steady-state amplification at ω_o, is quite clear: The cold collisionless model of the beam-plasma interaction predicts infinite amplification rate at ω_p, and therefore the spectral components of the source very near ω_p head for this level (∞) as $t \to \infty$. It is interesting to contrast the form of the growth in Eq. 8 with the more usual absolute instability formed from pinching poles. In the latter case, the asymptotic growth with time is as $\exp(\alpha t)$, with the same α at every position z; in the present case, the response grows in time at a rate that depends on z.

The present refinements on stability criteria are chiefly of theoretical, as opposed to practical, significance, since a realistic plasma model should include temperature and/or collisional effects if the one-dimensional assumption is retained. As an example, in the limit of a very small collision frequency, γ_c, and zero plasma temperature, we can carry over the previous results by replacing ω_p with $\omega_p(1+j\gamma_c/2\omega)$ everywhere in the equation above. The essential singularity is now displaced into the upper-half ω-plane, and we can show that $\psi(t,z)$ remains bounded as $t \to \infty$. It is interesting to note, however, that the saddle-point evaluation of $\psi(z,t)$ in Eq. 8 now shows that

$$\psi_s(z,t) \sim \exp\left(-\frac{\gamma_c}{2}\tau + \frac{3\sqrt{3}}{4}(k_b z)^{2/3}(\omega_p\tau)^{1/3}\right). \tag{9}$$

That is, $\psi_s(t,z)$ grows for a (relatively) long time at the "collisionless" rate before the collisional damping sets in. The maximum of $\psi_s(z,t)$ is reached when

$$\tau_m = \left(\frac{\sqrt{3}}{2}\right)^{3/2} \frac{k_b z\left(\omega_p^{1/2}\right)}{(\gamma_c)^{3/2}}, \tag{10}$$

and is

$$\psi_{max}(z) \sim \exp\left[\left(\frac{\sqrt{3}}{2}\right)^{3/2}\left(\frac{\omega_p}{\gamma_c}\right)^{1/2} k_b z\right]. \tag{11}$$

This maximum of the response, ψ_{max}, can be shown to be identical to the maximum

steady-state amplification for small γ_c. A more detailed investigation of the transient aspects of this problem shows that the saddle-point contribution to ψ (ψ_s as given in Eq. 9) is the dominant part of the response until the time τ_m given in Eq. 10 (when $\psi_s = \psi_{max}$ as given in Eq. 11). For $\tau > \tau_m$, the pole at $\omega = \omega_o$ (which we have not yet discussed explicitly) becomes important at the time when ψ_s drops below the steady-state amplification level at the same source frequency, ω_o. That is, it can be shown that τ_m represents the minimum time for steady-state conditions to be reached at any position z.

In other physical situations, the effects of plasma temperature might be more important than collisions. It can be shown that the instability is again convective for small but finite plasma temperature and zero collision frequency. Finally, we should mention that Sturrock[3] pointed out some time ago that if one considers a cold drifting plasma interacting with a beam, then the point of zero plasma drift is the critical point between convective and nonconvective behavior.

To summarize, it has been illustrated by one example how caution must be exercised in stability criteria when an essential singularity of $F(\omega, z)$ exists on the real ω-axis. In these cases, the resolution of the convective or absolute nature of the instability may often rest on the inclusion of additional physical parameters in the model.

The importance of the essential singularities was first pointed out to the author by B. R. Kusse in a different example.

R. J. Briggs

References

1. The notation in this report follows R. J. Briggs, Electron-Stream Interaction with Plasmas (The M.I.T. Press, Cambridge, Mass., 1964), p. 32.
2. Ibid., p. 22.
3. P. A. Sturrock, "Kinematics of Growing Waves," Phys. Rev. 112, 1488-1503 (1958).

10. MOTION OF CHARGED PARTICLES IN MAGNETIC MIRROR FIELD IN THE PRESENCE OF A RADIAL TIME-VARIANT ELECTRIC FIELD

The presence of a uniform RF electric field affects the gyrating motion of a charged particle in a uniform magnetic field perpendicular to the RF electric field according to the frequency of the RF field (ω). For $\omega \gg \omega_B$ (ω_B is the frequency of gyration) and $\omega \ll \omega_B$, there is no time-average exchange of energy between the electromagnetic field and the particle. But for $\omega = \omega_B$, the particles gain energy from the field, because of the cyclotron resonance. Those particles that start in phase with the field will gain energy indefinitely, until radiation losses and relativistic effects become significant. Those starting out of phase will lose energy until they are brought into phase with the RF field.

If the magnetic field is nonuniform, the resonance interaction will be modified. Transverse gradients of the magnetic field produce a frequency of gyration that depends on radial position. Longitudinal gradients add an acceleration along the field lines and, as in the case of a magnetic mirror, may cause reflections (see Appendix A). The acceleration experienced by a particle will also depend on its radial position, because of the radial gradients of the electric field. The phase relationship between the gyrating particle and the applied RF field is thus altered from the uniform field case.

In general, there are many mechanisms in a plasma which change the phase relationship between the particles and the field. It is our interest to study the effect of the nonuniformity of the fields on the energy exchange between the RF field and a single particle.

The trajectories of the particles are obtained by numerical integration of the normalized nonrelativistic equations of motion. The fields that are used are a magnetic mirror field and an electric field, attributable to an oscillating line charge. The frequency of the electric field corresponds to an average cyclotron frequency at the midplane of the mirror. The trajectories to be studied can be classified as follows: Class I, Particles that stay in the midplane; Class II, Particles that stay close to the midplane; and Class III, Particles that move far from the midplane.

Results

A measure of the inhomogeneity of the magnetic field is given by the mirror ratio (the ratio of the maximum to the minimum value of the field along the axis) and the aspect ratio (L/L_o - the ratio of the distance between the points of maximum field strength along the axis to the maximum radial distance of interest). The ratio of characteristic Larmor radius for the particle motion to the radial dimension of the system $\left(R_L = \frac{mV_o}{qB_o}\frac{1}{L_o}\right)$ gives a measure of the portion of space that the particle samples. The

ratio of the energy in the electric field to the initial energy of the particle is given by $\underset{\sim}{K}/R_L$, where $\underset{\sim}{K}$ is the normalized constant associated with the field (see Appendix A). The frequency of the applied electric field is the controlling parameter for the exchange of energy between particle and field. The corresponding values are given in Appendix B.

Trajectories of Class I

See Fig. XIII-31. (Also, see Appendix B.) The initial velocity is in phase with the field. The energy increases monotonically with time. The normalized radial position

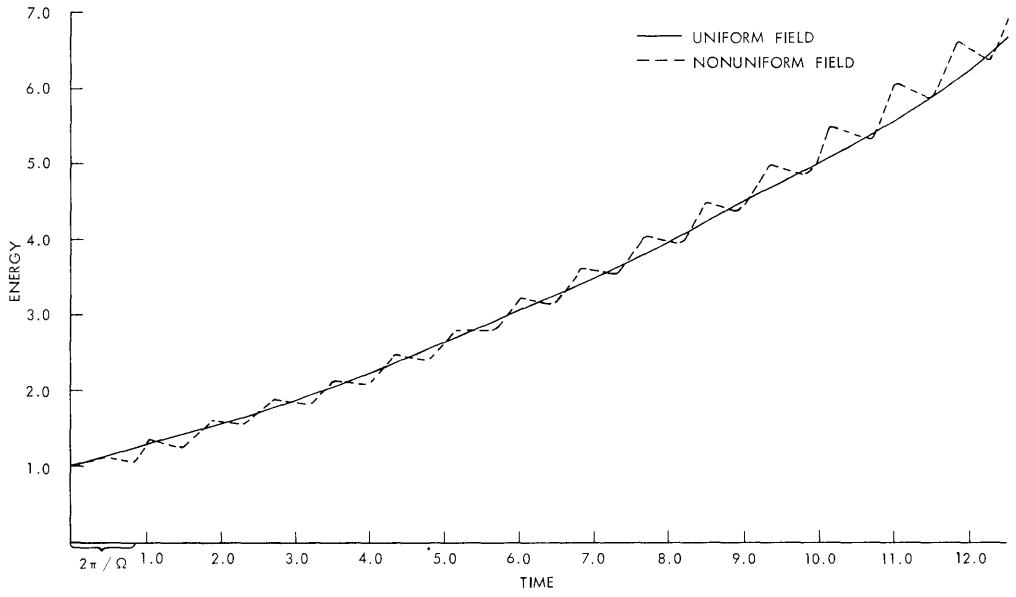

Fig. XIII-31. Energy as a function of time for a particle that stays in the midplane and starts in phase with the electric field, compared with a particle starting in phase (for the cyclotron-resonance case) in uniform electric and magnetic fields.

of the guiding center oscillates about a value of approximately 0.44, and the amplitude of this oscillation reaches values of approximately 0.1. After $T \approx 8.26$ (approximately 10 cyclotron periods), the particle has completed one revolution around the axis. As time increases, the energy gained by the particle becomes larger than that predicted for the uniform fields.

See Fig. XIII-32. The initial velocity is out of phase with the electric field. The energy decreases up to a time T = 7.05 (~8.5 cyclotron periods). For times greater than this the energy increases, since the particle has been brought into phase with the field. The normalized radial position of the guiding center moves inward from an initial

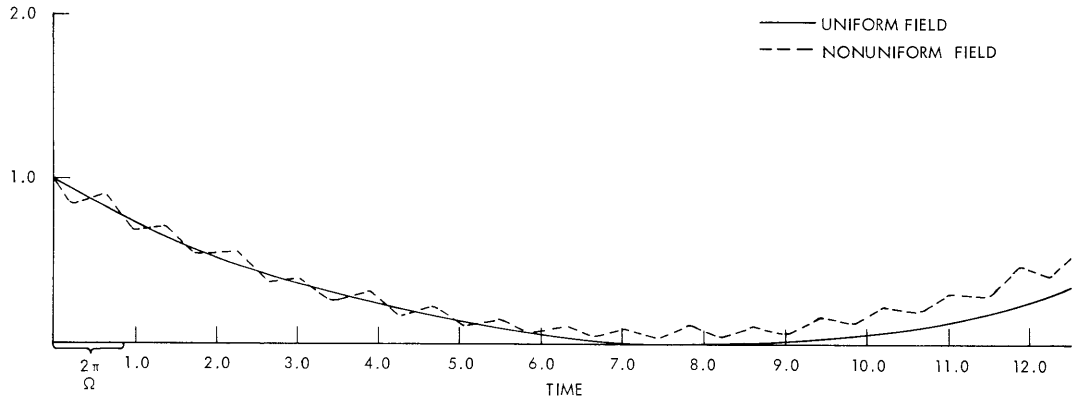

Fig. XIII-32. Energy as a function of time for a particle that stays in the midplane out of phase with the electric field, compared with the corresponding case in uniform fields.

position ~0.428 to an average value of approximately 0.4061. The variations about this value decrease as the energy decreases, and start to increase as the energy increases. After approximately 25.5 cyclotron periods, the particle has completed one revolution around the axis.

Trajectories of Class II

See Fig. XIII-33. The initial velocity is in phase with the field. The energy and the magnetic moment increase. The normalized radial position of the guiding center has an initial value of 0.428, and moves out to an average value of 0.45. The variations about this position reach values of approximately 0.1. The particle reflects at ~2.41 cyclotron periods (T = 5.0566), ~9.12 cyclotron periods, ~11.9 cyclotron periods, and 14.05 cyclotron periods. The z coordinate of the reflection points moves inward as the energy increases. For the first reflection the guiding center is located at $z \approx 0.0866$. By the time of the third reflection, the particle has completed one revolution around the axis.

See Fig. XIII-34. The initial velocity is out of phase with the field. The energy and the magnetic moment decrease until ~7.5 cyclotron periods (T = 5.778). For times greater than this, the energy and the magnetic moment increase. The normalized radial position of the guiding center is initially ~0.428, goes down to an average of 0.405 as the energy goes down, and increases back to an average of ~0.415 as the energy starts to increase. The particle is brought into phase between the first and second reflections. Thus, the z coordinate for the first reflection is farther away from the midplane than the others, since it corresponds to the reflection of lowest energy. The z coordinates of the reflection points move toward the midplane as energy increases. At ~17.05 cyclotron periods, the third reflection occurs, and the guiding center is at z = 0.1203, while

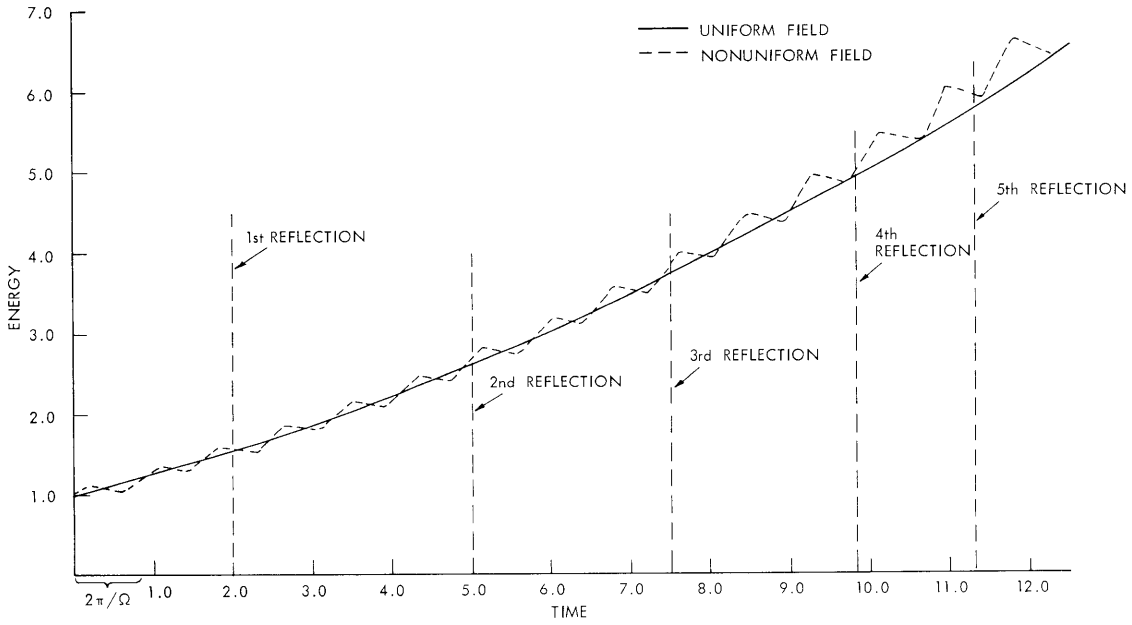

Fig. XIII-33. Energy as a function of time for a particle that stays close to the midplane and starts in phase with the electric field, compared with the corresponding case in uniform fields.

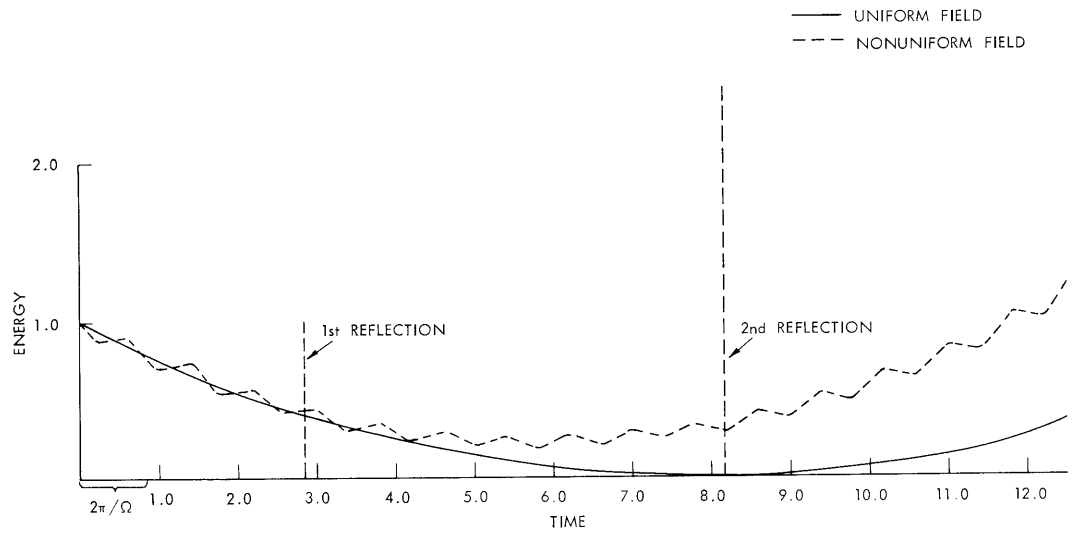

Fig. XIII-34. Energy as a function of time for a particle that stays close to the midplane and starts out of phase with the electric field, compared with the corresponding case in uniform fields.

for the first reflection it was at z = 0.167. At ~20.65 cyclotron periods, the particle's angular position is 5.81 radians (not having completed one revolution around the axis). The trajectories of particles that move far away from the midplane are now under study.

Appendix A. The Fields and Their Normalization in Computations

The magnetic field used for the caluclations is of the form

$$B_r = -B_o \alpha I_1 \left(\frac{2\pi r}{L}\right) \sin\left(\frac{2\pi r}{L}\right)$$

$$B_z = B_o\left[1 - \alpha I_o\left(\frac{2\pi r}{L}\right)\cos\left(\frac{2\pi r}{L}\right)\right],$$

where the mirror ratio Rm = $(1+\alpha)/(1-\alpha)$, L is the distance between the mirrors, and B_o is the field at r = 0, z = ±L/4. The electric field is given by

$$E_r = \frac{K}{r}(1+\cos\omega t) \qquad r \geq 0.1\ R_{max}$$

$$= \frac{K}{0.1\ R_{max}}(1+\cos\omega t) \qquad r \leq 0.1\ R_{max}$$

A way of producing an electric field of this type has been proposed by L. D. Smullin.[1]

The equations of motion are normalized by using as variables $\vec{V} = \vec{v}/V_o$, $\underset{\sim}{\vec{B}} = \vec{B}/B_o$, $\underset{\sim}{\vec{E}} = \vec{E}/v_o B_o/C$, $T = v_{ot}/L_o$, $\vec{R} = \vec{r}/L_o$, where L_o is a characteristic length (R_{max}), B_o is a characteristic value of the magnetic field (B(r = 0, z = ±L/4)), and v_o is a characteristic velocity (the initial velocity). Then the equations of motion are

$$R_L \frac{d\vec{V}}{dT} = \underset{\sim}{\vec{E}} + \vec{V} \times \vec{B}, \tag{1}$$

where $R_L = \frac{mv_o}{qB_o}\frac{1}{L_o}$ is the ratio of the characteristic Larmor radius to the characteristic length. The normalized fields are

$$\underset{\sim}{B}_r = -\alpha I_1\left(2\pi R\,\frac{L_o}{L}\right)\sin\left(2\pi Z\,\frac{L_o}{L}\right)$$

$$\underset{\sim}{B}_z = 1 - \alpha I_o\left(2\pi R\,\frac{L_o}{L}\right)\cos\left(2\pi Z\,\frac{L_o}{L}\right)$$

$$\underset{\sim}{E}_r = \underset{\sim}{K}\frac{1}{R}(1+\cos\Omega t),$$

where

$$\underset{\sim}{K} = \frac{K}{\frac{L_o V_o B_o}{C}}, \qquad \Omega = \frac{\omega}{(v_o/L_o)}$$

$$\Omega_B = \frac{\omega_B}{(V_o/L_o)} = \frac{\underset{\sim}{B}}{R_L}$$

For the uniform fields,

$$\underset{\sim}{E}_r = \frac{E_o}{\frac{v_o B_o}{C}} (1+\cos\Omega T); \qquad \vec{\underset{\sim}{B}} = \frac{\vec{B}}{B_o}.$$

The solution to Eq. 1, with uniform fields and $\Omega = \Omega_B$, is

$$V_R = V_r(0) \cos \Omega_B T + \left(V_o(0) + \frac{3}{2} \frac{\underset{\sim}{E}_o}{\underset{\sim}{B}} \right) \sin \Omega_B t + \frac{\underset{\sim}{E}_o}{2R_L} t \cos \Omega_B t$$

$$V_\theta = -V_r(0) \sin \Omega_B T + \left(V_\theta(0) + \frac{\underset{\sim}{E}_o}{\underset{\sim}{B}} \right) \cos \Omega_B t + \frac{\underset{\sim}{E}_o}{2R_1} t \sin \Omega_B T - \frac{\underset{\sim}{E}_o}{\underset{\sim}{B}}.$$

When $V_\theta(0) = 0$. The energy in the uniform field case can be approximated by

$$EN = V_R^2(0) + V_R(0) \frac{\underset{\sim}{E}_o}{R_L} t + \frac{\underset{\sim}{E}_o^2}{4R_L} 2t^2.$$

When $V_R = 0$, this approximation is not useful because the cross terms become important in carrying the information about the initial phase difference.

Appendix B. Parameters Used in the Computation

All computations have been done by using the following values.

Mirror Ratio = 1.5

$R_L = 0.1$

$K = 0.01$ (which corresponds to an E_o (in the uniform case) of 0.025)

$\frac{L}{L_o} = 3.0$

$\Omega = 7.6.$

The following trajectories have been studies.

Class I. Particles that stay in the midplane. Initial position – $R_o = 4$

$\theta_o = 0.0, \quad z_o = 00$

(a) $V_o = 1.0\ i_r$ – in phase with the RF field

(b) $V_o = -1.0\ i_r$ – out of phase with the RF field

(c) $V_o = 1.0\ i_\theta$ – out of phase with the RF field

(d) $V_o = -1.0\ i_\theta$ – out of phase with the RF field.

Class II. Particles that stay close to the midplane. Same initial position.

(a) $V_o = 0.9949874\ i_r + 0.1\ i_z$

(b) $V_o = -0.9949874\ i_r + 0.1\ i_z$

(c) $V_o = 0.9949874\ i_\theta + 0.1\ i_z$

(d) $V_o = -0.9949874\ i_\theta + 0.1\ i_z$.

O. Lopez, J. G. Siambis

References

1. L. D. Smullin, Quarterly Progress Report No. 80, Research Laboratory of Electronics, January 15, 1966, pp. 111-113.

XIII. PLASMAS AND CONTROLLED NUCLEAR FUSION*

B. Applied Plasma Physics Related to Controlled Nuclear Fusion

Academic and Research Staff

Prof. D. J. Rose
Prof. T. H. Dupree
Prof. L. M. Lidsky
Prof. E. P. Gyftopoulos
Prof. S. Yip
Dr. K. Chung

Graduate Students

K. R-S. Chen
H. Ching
D. G. Colombant
R. W. Flynn
R. A. Hill
M. Hudis
W. H. Manheimer
G. R. Odette
L. C. Pittenger
A. Sugawara
C. E. Wagner
A. Watanabe

1. EXPERIMENTAL STUDY OF HOLLOW-CATHODE DISCHARGE ARC PLASMA

We have continued the study of the highly ionized Argon plasma produced by the hollow-cathode discharge arc (HCD).[1] This study includes measurement of the ion temperature, and observation of the plasma oscillations with correlation techniques used.

Ion Temperature

We have measured the ion temperature by observing the Doppler broadening of a singly ionized Argon spectral line at 4806 Å. A Fabry-Perot interferometer was designed and built which has a resolving power of 7.57×10^5. During the operation of the interferometer, the spacing between the plates was fixed, and the pressure of gas (N_2) of the interferometer cell was varied to change the index of refraction. A typical profile of the spectral line is shown in Fig. XIII-35, in which the phototube output is traced simultaneously with the pressure of the cell. Analyzing the spectral profile according to the expression for the Doppler half-width,

$$\delta\lambda_D = \lambda_o (\ln 2) \left(\frac{2kT_i}{mc^2}\right)^{1/2}, \tag{1}$$

where λ_o is 4806 Å for our case, we obtained the experimental ion temperature. In the actual analysis, we included the Zeeman splitting of the spectral line caused by the presence of a strong axial magnetic field. The typical datum shown in Fig. XIII-35 represents an ion temperature of 0.41 eV, as compared with the electron temperature of 5.82 eV measured by the Langmuir probe.

Estimating the charge transfer cross section by extrapolating the available values (for $20\ \text{eV} \geq kT_i \geq 1\ \text{eV}$) into the energy range for this experiment, we computed the

*This work was supported by the National Science Foundation (Grant GK-1165).

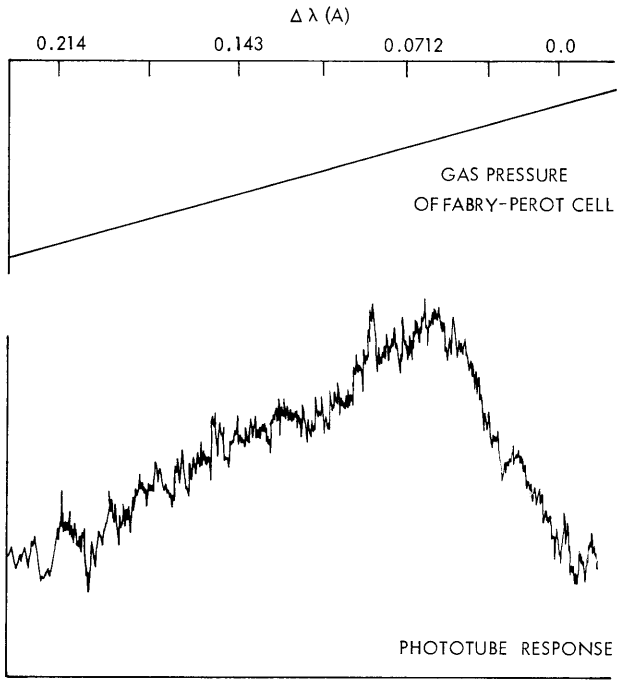

Fig. XIII-35.

Spectral-line profile obtained by a Fabry-Perot interferometer. ($r = 0 \pm 0.2$ cm, $T_e = 5.28$ eV, $T_i = 0.41$ eV).

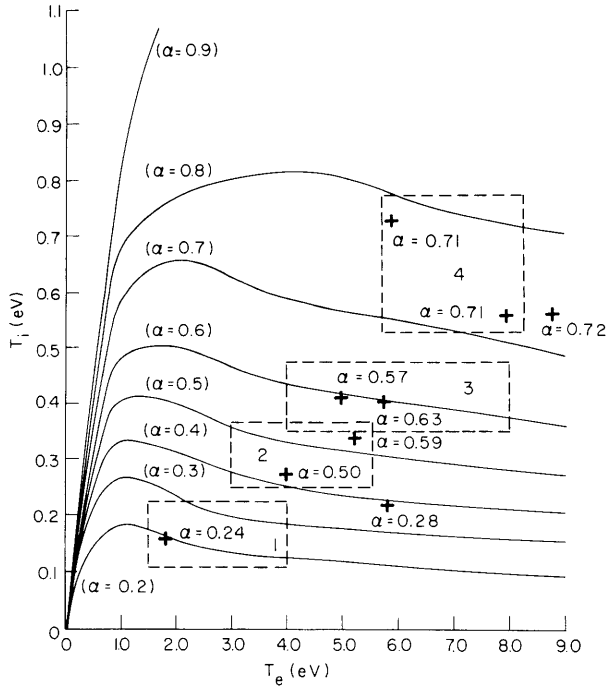

Fig. XIII-36. Ion temperature vs electron temperature with different values of α (degree of ionization). The typical experimental points are represented by + and corresponding α values. In region 1, B = 1.4 kGauss, r = 0.8 ± 0.2 cm; in region 2, B = 2.8 kGauss, r = 0.8 ± 0.2 cm; in region 3, B = 1.4 kGauss, r = 0 ± 0.2 cm, and in region 3, B = 2.8 kGauss, r = 0 ± 0.2 cm.

degree of inonization, α, as a function of the ion and electron temperatures.

$$\alpha = \frac{n_i}{n_i + n_o} = \left\{ 1 + \left(\frac{kT_e}{kT_i} - 1 \right) \frac{\sigma_{ie}}{\sigma_{io}} \right\}^{-1}, \tag{2}$$

where the collision cross section for energy transfer to ions from electrons, σ_{ie}, was replaced by $26/T_e^{3/2}\, T_i^{1/2}\, \text{Å}^2$, and σ_{io} is the charge transform cross section.

The direct experimental values of α can be obtained through the plasma density measurement by the probe and the background pressure reading. In Fig. XIII-36 we show a comparison between the values of α by plotting the experimental points in the $(T_i\text{-}T_e)$-plane. On the other hand, we can estimate the ion temperature by using the experimental value of α with the aid of relation (2). Within some restricted operation conditions of the HCD, we obtained an excellent agreement between the experimental and calculated ion temperatures (within 10% difference).

Plasma Oscillations

We have investigated the nature of the oscillations[2] when the plasma is unstable. Langmuir probe data are analyzed by obtaining autocorrelations and crosscorrelations electronically in quasi-real time. In Fig. XIII-37 we show an oscilloscope picture of the oscillations, and the autocorrelogram of the oscilloscope picture taken by the correlator. The autocorrelation of a signal $f_A(t)$,

$$R_A(\tau) = \frac{1}{T} \int_0^T f_A(t)\, f_A(t+\tau)\, dt, \tag{3}$$

can be used to get the power spectrum through the Fourier transformation. Figure XIII-37 shows the power spectrum (c) obtained by the Fourier transformation of (b). The averaging time, T, in this case is 5 seconds.

The crosscorrelation between two signals $f_A(t)$ and $f_B(t)$,

$$R_{AB}(\tau) = \frac{1}{T} \int_0^T f_A(t)\, f_B(t+\tau)\, dt, \tag{4}$$

can be used to get not only the extent of signal f_A in signal f_B, or vice versa, but also the clear phase lag between them.

In Fig. XIII-38 we show (a) the oscilloscope traces, (b) the crosscorrelogram, and (c) the Fourier transform of (b) of signals detected by two probes separated by 90° azimuthally. We note that in Fig. XIII-38c we have a single strong peak at 50.7 kHz, which indicates that the signals are due to an unstable rotating mode. The phase lag between the two signals shown in Fig. XIII-38b is clearly 180°, and thus we conclude that this particular oscillation is an m = 2 mode, and the fundamental frequency is 25.3 kHz,

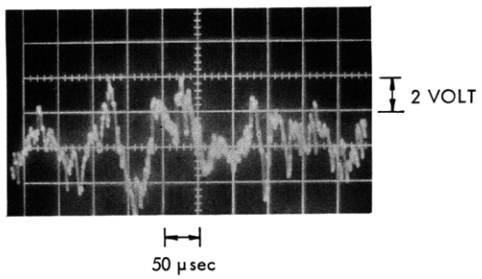

(a)

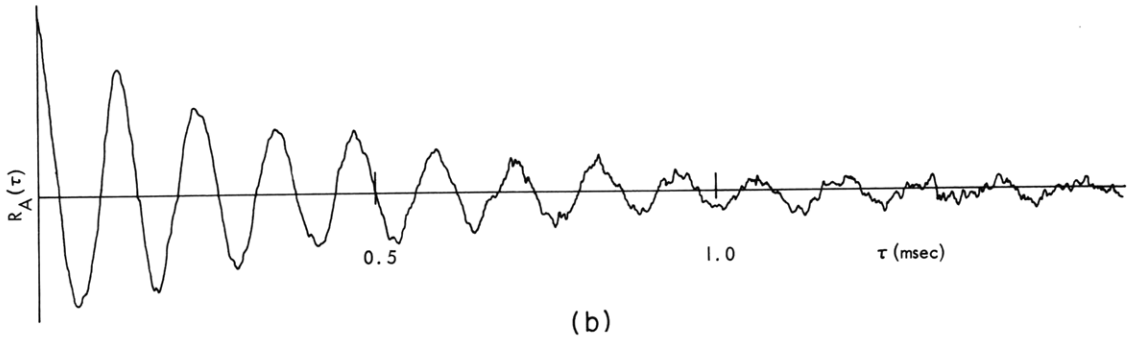

(b)

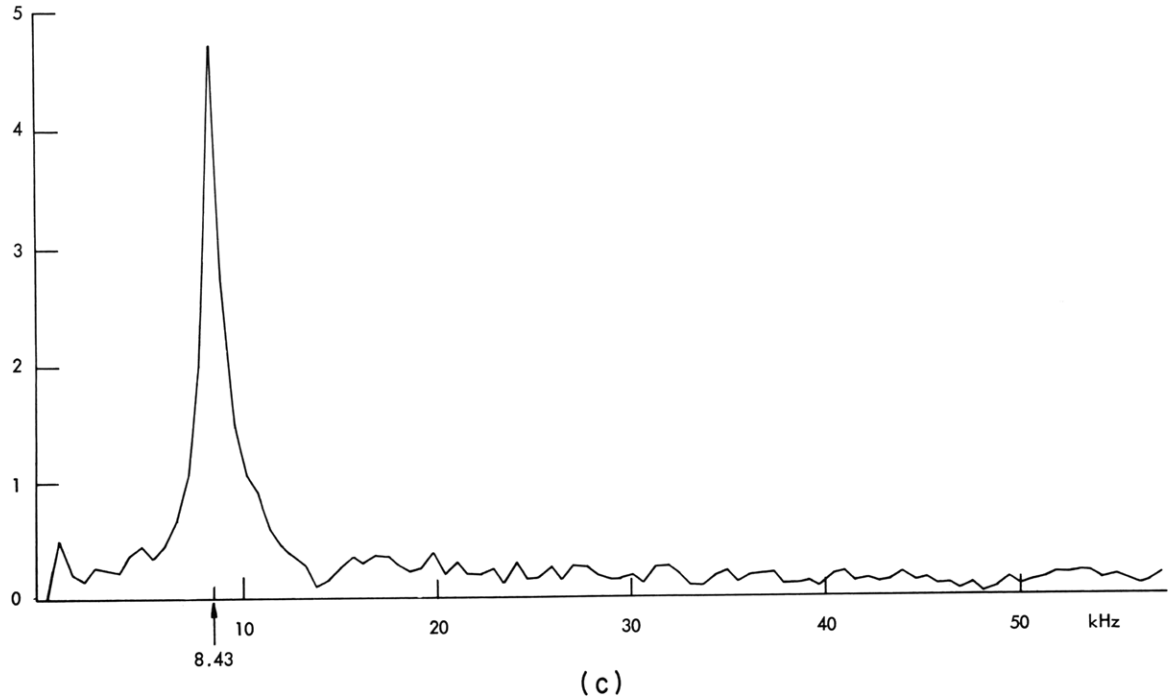

(c)

Fig. XIII-37. (a) Oscilloscope picture of the oscillation ($f_{app} \approx 9$ kHz).
(b) Autocorrelogram of (a).
(c) Power spectrum of (b).

instead of 50.7 kHz. We also biased the probes near the electron-saturation and ion-saturation regions, and obtained the signals. By employing many probes azimuthally

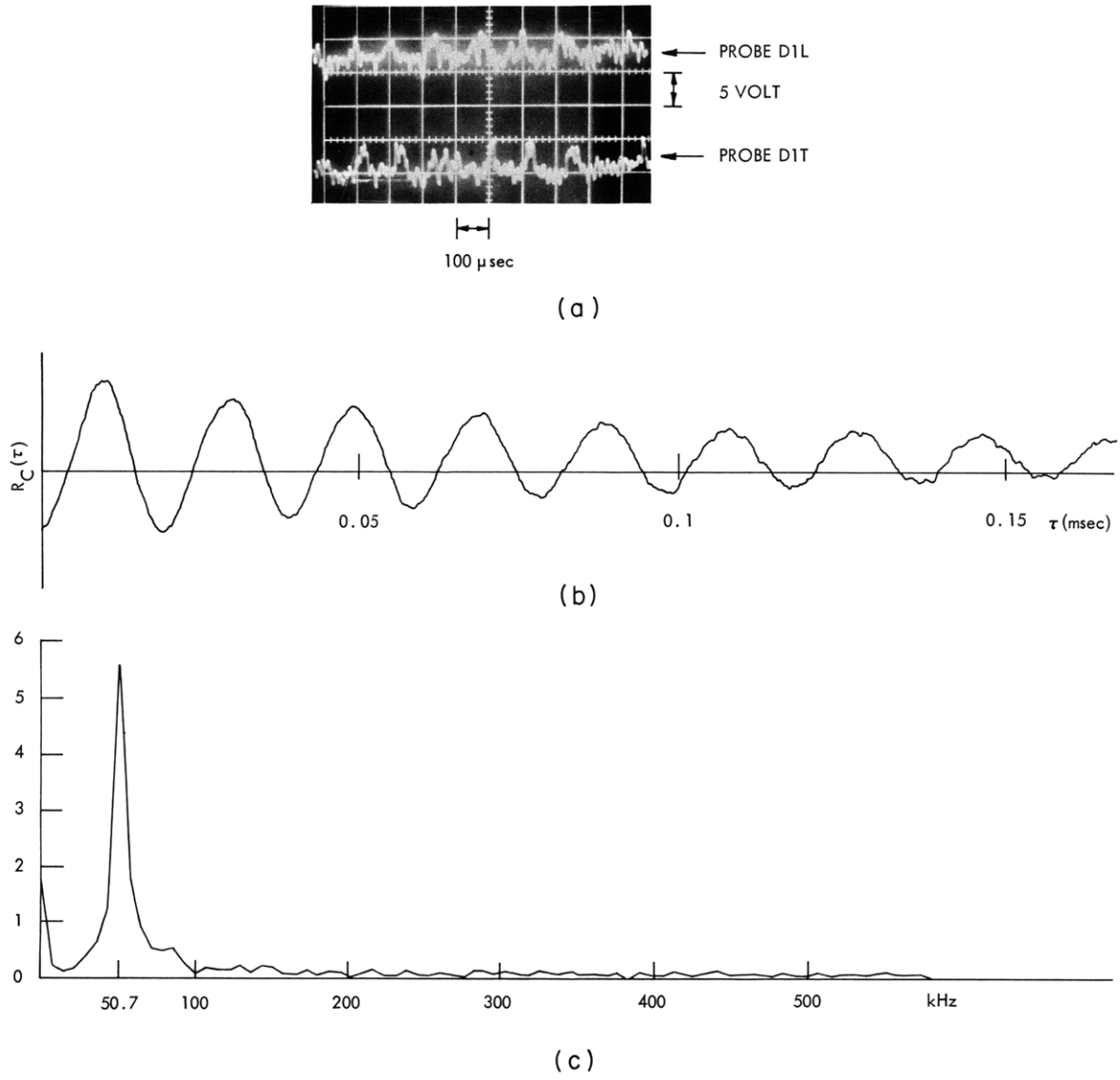

Fig. XIII-38. (a) Oscilloscope pictures of the oscillation ($f_{app} \approx 50$ kHz) picked up by two probes separated by 90° azimuthally.
(b) Crosscorrelogram of (a).
(c) Fourier transform of (b).

and axially separated, and moving the probes radially, we have obtained further information about the oscillations in the unstable plasma.

In Table XIII-1 we summarize data from the crosscorrelograms. Because of the strong dependency of the oscillations on the source magnetic field, we list the current

Table XIII-1. Characteristics of oscillations in HCD.

I_s (A)	r (in)	Azimuthal Probe Separation	Probe Bias	f_{app} (kHz)	m (experimental)
120	3/8	90°	Floated	8.9	0.92
120	6/8	90°	Floated	8.8	-1.0
150	6/8	45°	Ion Saturated	8.6	-0.87
137	1	45°	Floated	9.0	-0.82
137	1	90°	Floated	9.0	-1.1
50	3/8	45°	Floated	53.0	-2.1
50	3/8	90°	Floated	53.0	-2.0
50	6/8	90°	Floated	52.3	0
50	7/8	90°	Floated	50.0	0
50	9/8	90°	Floated	53.5	0

to the source magnetic coils, I_s. The apparent frequency is f_{app}, and r represents the radial positions of the Langmuir probes.

In Table XIII-1 we have chosen the positive direction of θ as the counterclockwise direction looking along the axial magnetic field, that is, from the anode to the cathode. To determine the helicity of the mode, we obtained crosscorrelations between probes separated along the magnetic field lines. We could not detect any phase lag between them. From Table XIII-1 we construct the following model for the unstable modes: (a) the low-frequency oscillation ($f_{app} \approx 9$ kHz) has mode m = 1, and reverses azimuthal direction at an intermediate plasma radius, and is stronger at the boundary; (b) the high-frequency oscillation ($f_{app} \approx 50$ kHz), mode m = 2, is strong near the center of the plasma column, and is weak and nonrotating in the outer region. The reversal of azimuthal direction of the low-frequency oscillation agrees with the $\overline{E} \times \overline{B}$ direction obtainable from the space potential measurement,[3] which is reproduced in Fig. XIII-39. In Fig. XIII-40 we

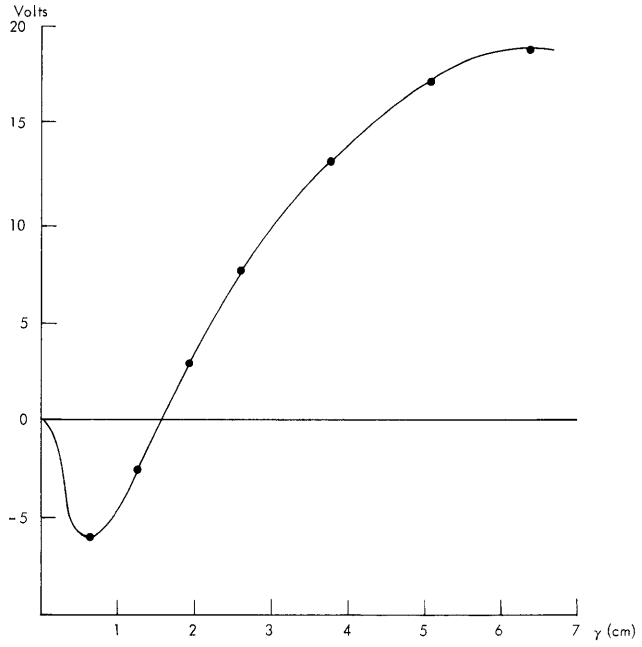

Fig. XIII-39. Radial profile of the plasma potential in an unstable regime.

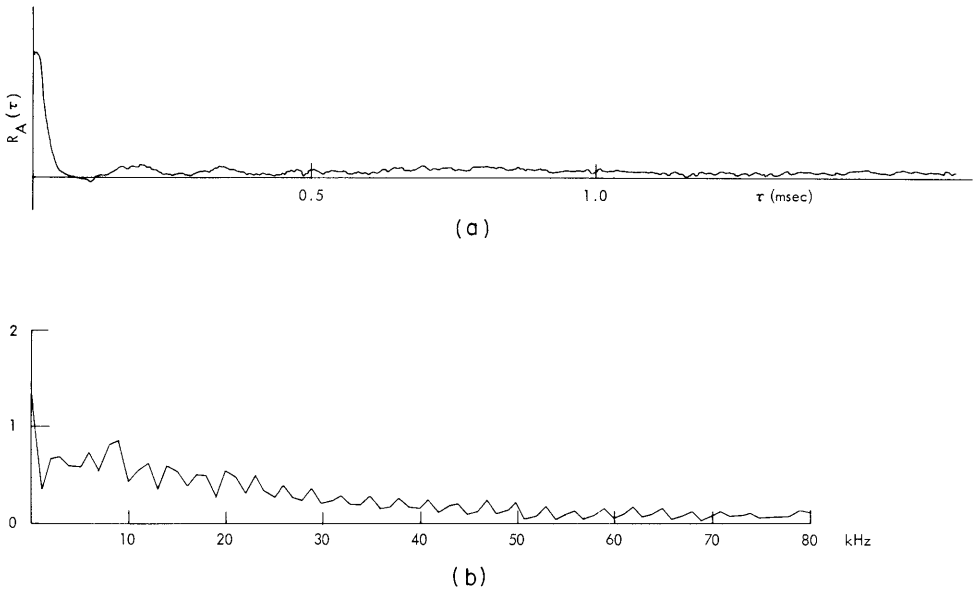

Fig. XIII-40. (a) Autocorrelogram in a "quiet" plasma.
(b) Power spectrum of (a).

show the remarkably clear autocorrelogram, and the power spectrum in the "quiet" plasma. In Fig. XIII-40 we see no oscillations except the noise.

M. Hudis, D. J. Rose, J. Small, K. Chung

References

1. J. C. Woo, L. M. Lidsky, and D. J. Rose, Quarterly Progress Report No. 76, Research Laboratory of Electronics, M. I. T., January 15, 1965, pp. 130-133.
2. K. Chung, Quarterly Progress Report No. 84, Research Laboratory of Electronics, M. I. T., January 15, 1967, pp. 159-163.
3. J. C. Woo, Ph. D. Thesis, Department of Nuclear Engineering, M. I. T., 1966, p. 89.

XIII. PLASMAS AND CONTROLLED NUCLEAR FUSION

C. Plasma Magnetohydrodynamic Flows, Waves, and Instabilities

Academic and Research Staff

Prof. W. P. Allis Prof. H. A. Haus

Graduate Students

C. A. McNary K. R. Edwards

1. MAGNETOHYDRODYNAMIC WAVE PROPAGATION TRANSVERSE TO MAGNETIC FIELD

When a magnetic field exists in a compressible fluid with a finite electric conductivity, the evolution of magnetic field disturbances can be strongly coupled to fluid-motion fluctuations if these events occur with time scales that are shorter than the magnetic field relaxation time for the fluid. In such an electromechanically coupled medium, an increase in apparent fluid stiffness occurs with an increase in magnetic field strength. This causes an increase in the phase velocity of compressional wave modes traveling transverse to the magnetic field – commonly called magnetoacoustic waves. These waves are described by a combination of the quasi-static Ampère law for a magnetic system, Faraday's law, Ohm's law (with $\omega_c \ll \nu$), conservation laws for mass and momentum, and a thermodynamic equation of state. For a highly conductive, homogeneous, isotropic, ideal gas approximately described by an adiabatic equation of state, the aforementioned combination yields the magnetoacoustic wave equation

$$\frac{\partial^2 \psi}{\partial t^2} = c^2 \frac{\partial^2 \psi}{\partial \chi^2} \tag{1}$$

$$c^2 = s^2 + a^2, \quad s^2 = \gamma \frac{p_o}{\rho_o} \quad \text{and} \quad a^2 = \frac{B_o^2}{\rho_o \mu}.$$

But this equation does not hold for a collision-dominated, partially ionized plasma where fluid motions occur with a time scale comparable with the magnetic field relaxation time, where fluctuations in conductivity accompany wave motion, and an equilibrium current density exists. This report is concerned with such a medium and the waves that it can support.

Physical assumptions incorporated in the mathematical model to be developed are

*This work was supported principally by the National Science Foundation (Grant GK-1165).

Table XIII-2. Physical assumptions, coordinate system, and glossary of symbols.

Assumptions

Homogeneous, isotropic, one-fluid model. Knudsen number «1.

$$\frac{\omega}{\nu}, \frac{\nu\omega}{\omega_p^2}, \frac{\mu_i}{\mu_e}, c[\mu\epsilon]^{1/2}, \frac{\rho_o k^2 \nu_k}{\sigma_o B_o^2}, \frac{k^2 K_\sigma T_o}{\alpha\left(J_o^2/\sigma_o\right)} \ll 1$$

$$\frac{\nu}{\nu_{ee}} < 1$$

The equilibrium (uniform) current density flowing in the plasma is assumed to be returned back through the plasma by evenly distributed wires, infinite in number and infinitesimal in thickness so as not to disturb the plasma flow and so as to ensure a uniform magnetic field.

Coordinate System

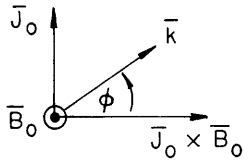

$$\bar{i}_p \cdot \bar{k} = k$$

$$(\bar{i}_t \times \bar{k}) \cdot \bar{B}_o = kB_o$$

The natural and constituent laws are linearized for small amplitude one-dimensional perturbations about an equilibrium state. Equilibrium variables have a zero subscript unless otherwise noted.

Glossary

Symbol	Definition	Symbol	Definition
B	magnetic field	α_o	n_{eo}/n_o
C_v, C_p	specific heats	γ	C_p/C_v
E_p, E_t	parallel, transverse electric fields	ϵ_i	ionization potential
i	$(-1)^{1/2}$	ϵ	permittivity
$\bar{i}_p, \bar{i}_t$	unit vectors $\perp B_o$	λ	wavelength
J	current density	μ	permeability
K_σ	thermal conductivity	μ_e, μ_i	electron, ion mobility
k	wave number	ν	$\nu_{ei} + \nu_{en}$
k_B	Boltzmann's constant	$\nu_{ee}, \nu_{ei}, \nu_{en}$	electron-electron, electron-ion, electron-neutral collision frequency
n	heavy-gas number density	ν_k	kinematic viscosity
n_e	electron number density	ρ	mass density
p	pressure	σ	conductivity
q	charge density	ϕ	angle of propagation
R	gas constant	Ω	Hall parameter
T	temperature	ω	wave frequency
t	time	ω_c	electron-cyclotron frequency
v_p, v_t	parallel, transverse velocity	ω_p	plasma frequency

given in Table XIII-2 along with a description of the coordinate system embedded in the moving plasma and a list of symbol meanings. The linearized equations of motion are Laplace-analyzed in space and time. Equivalently, the linearized natural and constituent laws are considered for one particular Laplace frequency and wave-number dependence. The variables are chosen to have the space-time dependence:

$$\text{Re } \zeta \exp(\omega t - \bar{k}\cdot\bar{r}).$$

In this report the wave number will be chosen as a real number, and the angular frequency will be sought analytically and numerically.

Conservation of Mass

$$\frac{\rho}{\rho_o} = \frac{k}{\omega} v_p. \tag{2}$$

Without equilibrium current density, these waves are of a purely compressional nature with $v_t = 0$.

Conservation of Momentum

$$\left(\frac{k}{\omega}\right) v_p = \left(\frac{k}{\omega}\right)^2 \gamma^{-1} s^2 \frac{p}{p_o} + i \frac{kJ_oB_o}{\rho_o\omega^2}\left(\frac{J}{J_o} - \cos\phi \frac{B}{B_o}\right) \qquad \text{(parallel component)} \tag{3a}$$

$$\left(\frac{k}{\omega}\right) v_t = -i \frac{kJ_oB_o \sin\phi}{\rho_o\omega^2} \frac{B}{B_o}. \qquad \text{(transverse component)} \tag{3b}$$

Except for propagation in the $\bar{J}_o \times \bar{B}_o$ direction, the velocity is rotational for a finite equilibrium current density. The rotational component of velocity results from the perturbation magnetic field interacting with the equilibrium current density so as to produce a force density that, in general, is unaligned with $\bar{k}$.

Ampère's Law

$$\frac{B}{B_o} = iI \frac{J}{J_o}; \qquad \bar{B} = \frac{\bar{B}_o}{B_o} B; \qquad I = \frac{\mu_o J_o}{kB_o}. \tag{4}$$

The current perturbation is in the transverse direction. The perturbation magnetic field is always aligned with the equilibrium magnetic field for plane wave propagation transverse to the equilibrium field.

Faraday's Law

$$\frac{\sigma_o}{J_o} E_t = -\frac{\sigma_o B_o(\omega/k)}{J_o} \frac{B}{B_o}. \tag{5}$$

Modified Ohm's Law

$$\Omega_o \cos\phi \frac{\Omega}{\Omega_o} - \Omega_o \frac{J}{J_o} = \frac{\sigma_o}{J_o} E_p - \frac{\sigma_o B_o}{J_o} v_t + (\Omega_o \cos\phi + \sin\phi) \frac{\sigma}{\sigma_o} \qquad \text{(parallel component)} \tag{6a}$$

$$\frac{J}{J_o} + \Omega_o \sin\phi \left(\frac{\Omega}{\Omega_o}\right) = \frac{\sigma_o}{J_o} E_t + \frac{\sigma_o B_o}{J_o} v_p + [\Omega_o \sin\phi - \cos\phi] \frac{\sigma}{\sigma_o} \qquad \text{(transverse component)} \tag{6b}$$

Equation 6b expresses the resistive-inductive nature of the medium. By using Eqs. 4 and 5, Eq. 6b can be rewritten in the form

$$\frac{J}{J_o}[1+iR_m] = -\Omega_o \sin\phi \left(\frac{\Omega}{\Omega_o}\right) + \frac{\sigma_o B_o}{J_o} v_p + [\Omega_o \sin\phi - \cos\phi] \frac{\sigma}{\sigma_o}. \tag{6c}$$

The right-hand side of (6c) represents a change in the electromotive force in the plasma continuum. The current variation lags this emf, as it would in a lossy inductor. The first term on the right of (6c) produces current variations as a result of changes in Hall parameter. That is, changes in the magnetic field and mass density cause the ratio of ω_c and ν to change, with the result that there is a repositioning of the equilibrium current density vector with respect to the electric field vector. The second term on the right of (6c) represents the conventional current variation associated with wave motion and produces wave damping. The last term on the right of (6c) is a current variation attributable to conductivity fluctuations. If the first and third terms more than cancel out the damping effects of the second term, wave growth may result — but not necessarily.

Thermodynamic Equation of State

$$\frac{p}{p_o} = \frac{\rho}{\rho_o} + \frac{T}{T_o}. \tag{7}$$

Conservation of Energy

$$\frac{T}{T_o} = \frac{R}{C_v}\left(\frac{k}{\omega}\right) v_p + i\left(\frac{k}{\omega}\right) c\gamma H\left[2\cos\phi \frac{J}{J_o} - \frac{\sigma}{\sigma_o}\right]; \quad H = \frac{J_o^2/\sigma_o}{kc\rho_o C_p T_o}. \tag{8}$$

The second and third terms on the right of Eq. 8 represent small changes in Joule heating. If these changes are in phase with temperature, wave growth may result — but again not necessarily.

Conductivity

$$\frac{\sigma}{\sigma_o} = \frac{n_e}{n_{eo}} - \frac{\nu}{\nu_o}. \tag{9}$$

Collision Frequency

$$\frac{\nu}{\nu_o} = \frac{\nu_{ei_o}}{\nu_o}\left(1 - \frac{1}{2\ln\Lambda_o}\right)\frac{n_e}{n_{eo}} + \frac{\nu_{en_o}}{\nu_o}\frac{\rho}{\rho_o} + \left[\frac{3}{2}\frac{\nu_{ei_o}}{\nu_o}\left(1 - \frac{1}{\ln\Lambda_o}\right) - \frac{1}{2}\frac{\nu_{en_o}}{\nu_o}\right]\frac{T}{T_o}$$

$$\Lambda_o = 12\pi\left(\frac{\epsilon k_B T_o}{e^2}\right)^{3/2} n_{eo}^{-1/2} \tag{10}$$

Cross sections for electron-neutral collisions are assumed to be constant.

Saha's Equation

$$\frac{n_e}{n_{eo}} = \left(\alpha + \frac{3}{4}\right)\frac{T}{T_o} + \beta\frac{\rho}{\rho_o}$$

$$\alpha = \frac{\epsilon_i}{2k_B T_o}\left(1-\alpha_o^2\right) - \frac{3}{4}\alpha_o^2; \qquad \beta = \frac{1}{2}\left(1+\alpha_o^2\right). \tag{11}$$

Equation 11 represents the balance between production and removal of free electrons for a Maxwellianized gas.

Hall Parameter

$$\frac{\Omega}{\Omega_o} = \frac{B}{B_o} - \frac{\nu}{\nu_o}. \tag{12}$$

Since, for the case at hand, the perturbation and equilibrium magnetic fields are vectorially aligned, the small amplitude changes in Hall parameter and magnetic field are also aligned, and thus the Hall parameter changes can be described here in a single scalar equation.

The thirteen linearized equations of motion and state presented above govern the thirteen small amplitude perturbations (v_p, v_t, p, ρ, T, J, E_p, E_t, B, n_e, ν, σ, Ω). Also, there is a fourteenth equation representing Gauss's law for small-amplitude charge density, but it is coupled to the other thirteen equations only through one of its two variables.

Gauss' Law

$$\frac{\sigma_o E_p}{J_o} = i\left(\frac{q_o}{J_o}\frac{\sigma_o/\epsilon_o}{k}\right)\frac{q}{q}. \tag{13}$$

Table XIII-3. Dispersion relation.

$$\omega_n^4 + \omega_n^3\{-iH\gamma C_4 - iR_m^{-1} + \Omega_o I R_m^{-1}\sin\phi\}$$

$$+ \omega_n^2\{-iI(1-\mathcal{R})\cos\phi - HR_m^{-1}\Omega_o I\gamma C_4 \sin\phi - 1 + HR_m^{-1}(X_{21} - \Omega_o X_{22})\}$$

$$+ \omega_n^1\left\{iH[\mathcal{R}\Omega_o X_{11} + \mathcal{R}X_{12} + \gamma C_4] + iR_m^{-1}\mathcal{R} + IR_m^{-1}[(1-\mathcal{R})(X_{14}+\Omega_o) - \mathcal{R}\Omega_o\sin\phi]\right.$$

$$\left. + H\mathcal{R}[FC_4\cos\phi - I^{-1}X_{16}]\right\}$$

$$+ \omega_n^o\left\{iH\mathcal{R}R_m^{-1}F\Omega_o\left[X_{o4} + \left(\frac{\mathcal{R}}{1-\mathcal{R}}\right)\gamma^{-1}\xi_{13}\sin\phi\right] + H\mathcal{R}\left[R_m^{-1}(X_{o1}+\Omega_o X_{o2}) + H\Omega_o X_{o3}\right]\right\}$$

$$= 0$$

$$C_1 = -\beta/\cos\phi$$

$$C_4 = \left[1 - \frac{\nu_{ei_o}}{\nu_o}\left(1 - \frac{1}{2\ln\Lambda_o}\right)\right]\left(\alpha+\frac{3}{4}\right) - \left[\frac{1}{2}\left(\frac{\nu_{en_o}}{\nu_o}\right) - \frac{3}{2}\left(\frac{\nu_{ei_o}}{\nu_o}\right)\left(1 - \frac{1}{\ln\Lambda_o}\right)\right]$$

$$C_5 = \frac{1}{2} - \frac{\nu_{ei_o}}{\nu_o} - \frac{1}{2}\frac{\nu_{ei_o}}{\nu_o}\left(1 - \frac{1}{2\ln\Lambda_o}\right)$$

$$\xi_{13} = 2C_4 - C_5$$

$$\xi_{14} = 2\left(\alpha+\frac{3}{4}\right) - \beta$$

$$X_{o1} = \xi_{13}(1-2\cos^2\phi)$$

$$X_{o2} = 2\xi_{14}\sin\phi\cos\phi$$

$$X_{o3} = \frac{-C_p}{R}C_4\xi_{14}\sin\phi\cos\phi + \frac{C_p}{R}\xi_{13}\left(\alpha+\frac{3}{4}\right)\sin\phi\cos\phi$$

$$X_{o4} = \left(\alpha+\frac{3}{4}\right)\xi_{13}\sin\phi - C_4\xi_{14}\sin\phi$$

$$X_{11} = \left[\left(1+\frac{C_v}{R}\right)\left(\alpha+\frac{3}{4}\right) - \frac{C_v}{R}\xi_{14}\right]\sin\phi\cos\phi$$

$$X_{12} = \left[\xi_{13} - \frac{C_v}{R}C_5 - C_4\right]\cos^2\phi + \xi_{13}\sin^2\phi - \gamma C_4$$

$$X_{14} = \left[\gamma C_4 - 2\frac{R}{C_v}\right]\cos\phi$$

$$X_{15} = \frac{C_v}{R}\xi_{14}\sin\phi - \left(1+\frac{R}{C_v}\right)\left(\alpha+\frac{3}{4}\right)\sin\phi$$

$$X_{16} = \frac{C_v}{R}\xi_{13}\cos\phi$$

$$X_{21} = 2\gamma C_4\cos^2\phi - \gamma C_4$$

$$X_{22} = 2\gamma\left(\alpha+\frac{3}{4}\right)\sin\phi\cos\phi$$

$$\omega = \omega/kc$$

$$H = \frac{R}{C_p}FR_m^{-1}I = \frac{\left(J_o^2/\sigma_o\right)}{kc(\rho_o C_p T_o)}$$

$$\mathcal{R} = \left(\frac{S}{c}\right)^2$$

$$F = \gamma I\left(\frac{1-\mathcal{R}}{\mathcal{R}}\right) = \frac{J_o B_o}{p_o k}$$

The dispersion equation formed from the set of homogeneous equations (2) through (12) is of fourth degree in wave frequency. It is given in Table XIII-3. Analytic solutions of the dispersion equation are stated for two limiting cases which are motivated by physical insight. First, analytic solutions for the characteristic frequencies are obtained in the limit of low current density. This limit is suggested by the fact that parameter variations have a negligible effect for low current density and are uncoupled from the magnetoacoustic roots. Second, analytic solutions are obtained in the limit of slight fluid compressibility. This limit is motivated by a desire to uncouple the two magnetoacoustic roots in such a manner that the two remaining modes can be examined.

Low-Current Density Limit

This limit considers solutions to first order in current density such that $\frac{J_o B_o}{p_o k}, \frac{\mu J_o}{k B_o} \sim \mathcal{O}(\epsilon)$, $\epsilon \ll 1$. Furthermore, solution is facilitated by choosing a large magnetic Reynolds number, $R_m^{-1} = \frac{k}{\mu_o \sigma_o c} \sim \mathcal{O}(\epsilon)$, with the Alfvén and acoustic speeds of the same order of magnitude. The result is that for $-\pi/2 \leq \phi \leq \pi/2$:

$$\omega_1 = kc + i\left[\left(\frac{k^2}{2\mu\sigma_o}\right)\left(\frac{a}{c}\right)^2 - \frac{1}{2}\frac{(\bar{J}_o \times \bar{B}_o)}{k\rho_o c^2} \cdot \bar{k}c\right] \qquad \text{(positive magnetoacoustic mode)} \quad (14a)$$

$$\omega_2 = -kc + i\left[\left(\frac{k^2}{2\mu\sigma_o}\right)\left(\frac{a}{c}\right)^2 + \frac{1}{2}\frac{(\bar{J}_o \times \bar{B}_o)}{k\rho_o c^2} \cdot \bar{k}c\right] \qquad \text{(negative magnetoacoustic mode)} \quad (14b)$$

$$\omega_3 = i\left(\frac{k^2}{\mu_o \sigma_o}\right)\left(\frac{s}{c}\right)^2 \qquad \text{(magnetic diffusion mode)} \quad (14c)$$

$$\omega_4 = 0 \qquad \text{(parameter variations mode)} \quad (14d)$$

Only the positive magnetoacoustic mode exhibits an instability, and this occurs whenever

$$IR_m \cos\phi > 1, \qquad (15)$$

where the most unstable direction of propagation is along $\bar{J}_o \times \bar{B}_o$. This instability results from the fact that the small amplitude Lorentz force density is less than $\pi/2$ radians out of phase with the velocity perturbation of the wave. Joule-heating effects have no influence in this limit; $H \sim \mathcal{O}(\epsilon^3)$, $\epsilon \ll 1$. By way of elaboration, consider the case in which $\phi = 0$. For near perfect conductivity, $v_p B_o \cong \frac{\omega}{k} B$. Some phase relationships of the positive magnetoacoustic wave ($\phi = 0$) are demonstrated in Fig. XIII-41. But if the effects of finite conductivity are accounted for, then $E_t - v_p B_o = J/\sigma$,

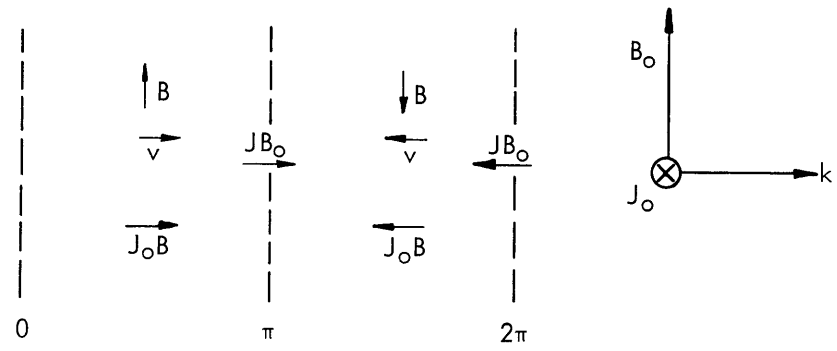

Fig. XIII-41. Phase relationships for positive magnetoacoustic mode for $\phi = 0$ and negligible resistivity.

or $v_p B = \left(\frac{a}{k}\right) B - i\left(\frac{k}{\mu\sigma_o}\right) B$, and then B leads v somewhat, as shown in Fig. XIII-42. The greater I becomes, the larger is the magnitude of J_oB relative to JB_o. It is the

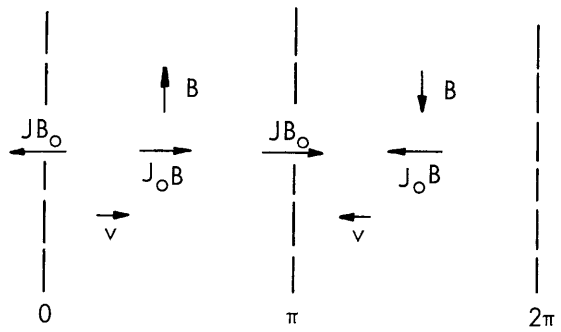

Fig. XIII-42. Phase relationships for positive magnetoacoustic mode for $\phi = 0$ and finite resistivity.

J_oB component of the Lorentz force density that is destabilizing. Furthermore, the larger R_m is, the less is the phase difference between velocity and magnetic field perturbations. To understand the inequality for some arbitrary angle ($|\phi| \leq \pi/2$), consider $\phi = \pi/2$. Here the inequality cannot be satisfied. In fact, the third term on the right side of (14a) disappears. This results from the fact that for $\phi = \pi/2$, J_oB acts in a direction orthogonal to v_p, and only serves to produce small amplitude motion transverse to the direction of propagation. With a more detailed analysis, it can be shown that this instability mechanism persists even when the criterion for the low-current-density limit is not met (with the same inequality (15) almost satisfied at a state of marginal stability). In summary, a physical mechanism for the instability of the positive magnetoacoustic mode has been exposed. Its existence depends upon the presence of a

finite current density, and does not depend upon parameter variations (though it may be influenced by them).

Slight Fluid Compressibility Limit

First, only incompressible phenomena are considered.

$$\omega_{1,2} \to \pm\infty \qquad \text{(positive, negative magneto-acoustic mode)} \qquad (16a,b)$$

$$\omega_3 = -\bar{k}\cdot\bar{s}_d + i(\zeta_1+\zeta_2); \quad \bar{s}_d = \frac{\bar{J}_o}{n_{eo}e}, \quad e = \text{electron charge} \qquad \text{(magnetic diffusion mode)} \qquad (16c)$$

$$\omega_4 = i(\zeta_1-\zeta_2)$$

$$\zeta_1 = \frac{1}{2}\frac{k^2}{\mu\sigma_o} + \frac{1}{2}\left[2\frac{(\bar{k}\times\bar{J}_o)\cdot\bar{B}_o}{kJ_oB_o} - 1\right]\frac{\alpha J_o^2/\sigma_o}{\rho_o C_p T_o} \qquad \text{(parameter variations mode)}$$

$$\zeta_2 = \left\{\zeta_1^2 + \left[2\frac{(\bar{k}\times\bar{J}_o)\cdot\bar{B}_o}{kJ_oB_o} - 1\right]\frac{\alpha J_o^2/\sigma_o}{\rho_o C_p T_o}\frac{k^2}{\mu\sigma_o}\right\}^{1/2}. \qquad (16d)$$

The physical meaning of (16c) and (16d) becomes more apparent in the limit of small magnetic Reynolds number, $R_m \sim \mathcal{O}(\epsilon)$.

$$\omega_3 = -\bar{k}\cdot\bar{s}_d + i\frac{k^2}{\mu\sigma_o} \qquad (17a)$$

$$\omega_4 = -i\left[\frac{2(\bar{k}\times\bar{J}_o)\cdot\bar{B}_o}{kJ_oB_o} - 1\right]\frac{\alpha J_o^2/\sigma_o}{\rho_o C_p T_o}. \qquad (17b)$$

The propagation of the magnetic diffusion mode simply represents the effect of electron drift, and therefore does not appear for $\phi = 0$. Magnetic field disturbances are swept along with the moving electron gas. The parameter variations mode indicates growth for $\phi = 0$ and decay for $\phi = \pi/2$. This is a result of having small-amplitude Joule-heating changes, respectively, in phase and out of phase with small temperature variations. For spatial variations along the $\bar{J}_o \times \bar{B}_o$ direction, the second term on the right of (8) dominates the third term, and growth results. For variations along the $\bar{J}_o$ direction, however, the second term does not contribute, since $\bar{J}$ is orthogonal to $\bar{J}_o$ and the third term, representing conductivity fluctuations, produces decay.

The solutions (17a) and (17b) can be further altered to include slight compressibility. For simplicity, assume $\phi = 0$ and also that I, R_m, $a^{-1} \sim \mathcal{O}(\epsilon)$ and $\frac{s^2}{a^2} \sim \mathcal{O}(1)$. Then, the slightly compressible solutions for the magnetic diffusion and parameter variations modes are

$$\omega_3^1 = a(\gamma-1)\, IR_m(1-\mathcal{R})\, kc + i\frac{k^2}{\mu_o \sigma_o} \tag{18a}$$

$$\omega_4^1 = \frac{a^2 J_o^2/\sigma_o}{\rho_o C_p T_o}(\gamma-1)\left(\frac{a}{c}\right)^2 I - i\frac{aJ_o^2/\sigma_o}{\rho_o C_p T_o}. \tag{18b}$$

The two unpaired modes, ω_3^1 and ω_4^1 take on wave propagation characteristics that reflect the existence of preferential directions in the medium. The physical effect causing propagation is similar for the two modes. For instance, in the parameter variations mode some relative phases of variables are indicated in Fig. XIII-43, with ΔT and $\Delta\sigma$

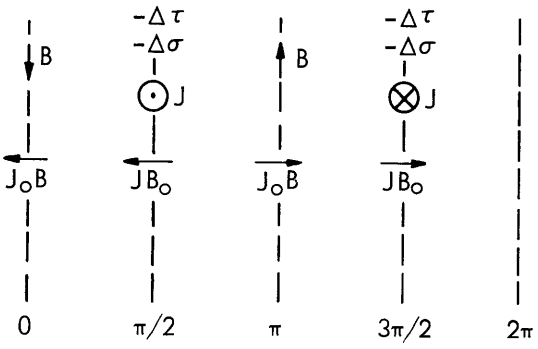

Fig. XIII-43. Dynamics of the parameter variations mode for $\phi = 0$ and slight compressibility.

indicating a positive small change in temperature and conductivity. The small changes in current density caused by conductivity fluctuations (which result from temperature changes) interact with the magnetic field. These forces, in turn, set up pressure gradients with peak pressure out of phase with the original conductivity fluctuations. These pressure gradients are accompanied by new temperature fluctuations, and so on, causing the pattern to shift in the $+\overline{J}_o \times \overline{B}_o$ direction. In (18b) the direction of propagation changes if either $\overline{J}_o$ or $\overline{B}_o$ is reversed, thereby reversing the preferential direction $\overline{J}_o \times \overline{B}_o$.

By means of a more extensive investigation, it can be shown that the basic concept of a magnetic diffusion mode and parameter variations mode that propagate remains valid even when the assumptions of Eqs. 18a and 18b are not met. Furthermore, it can

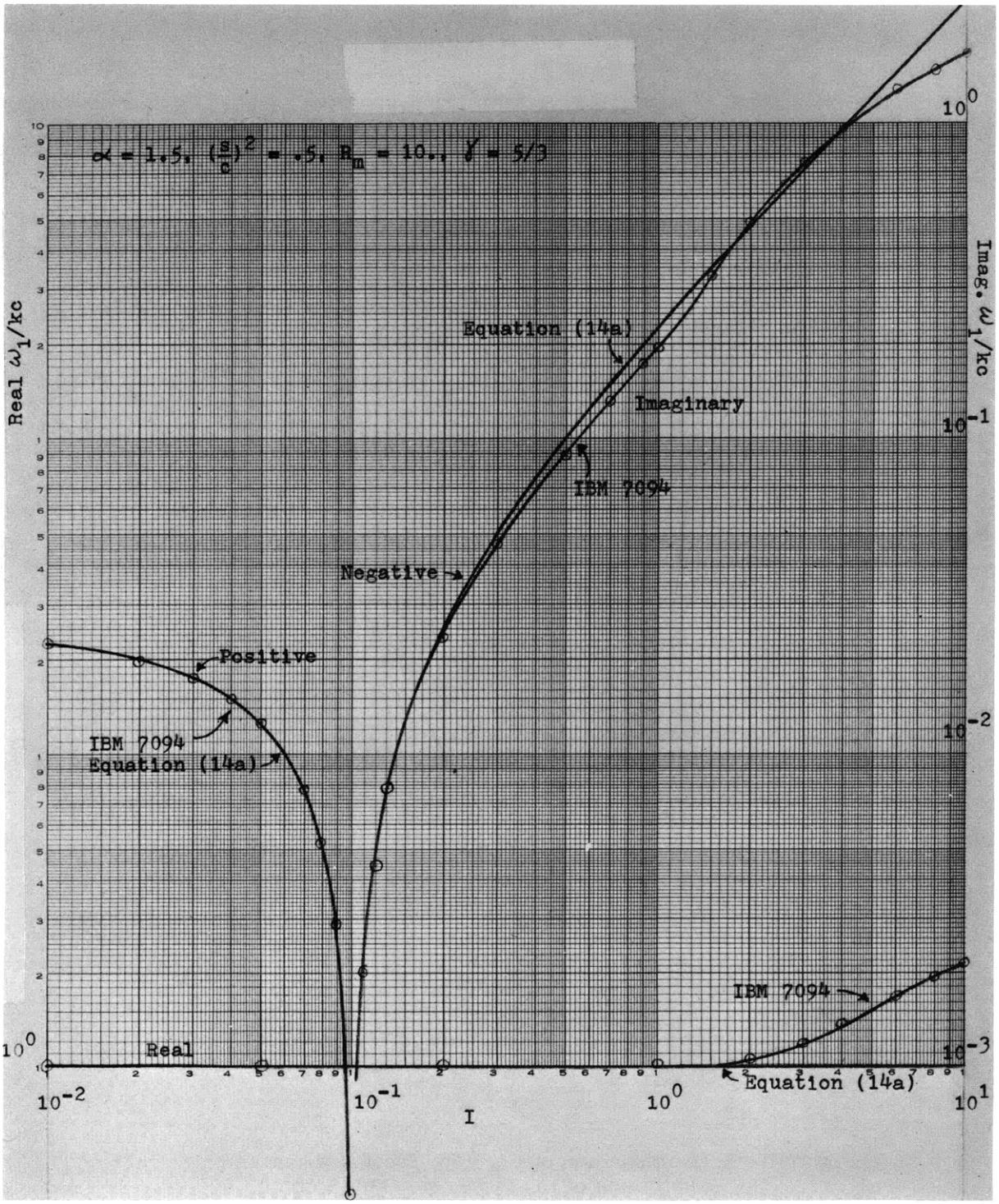

Fig. XIII-44. Comparison of Eq. 14a, for $\phi = 0$, with numerical solutions of the dispersion relation.

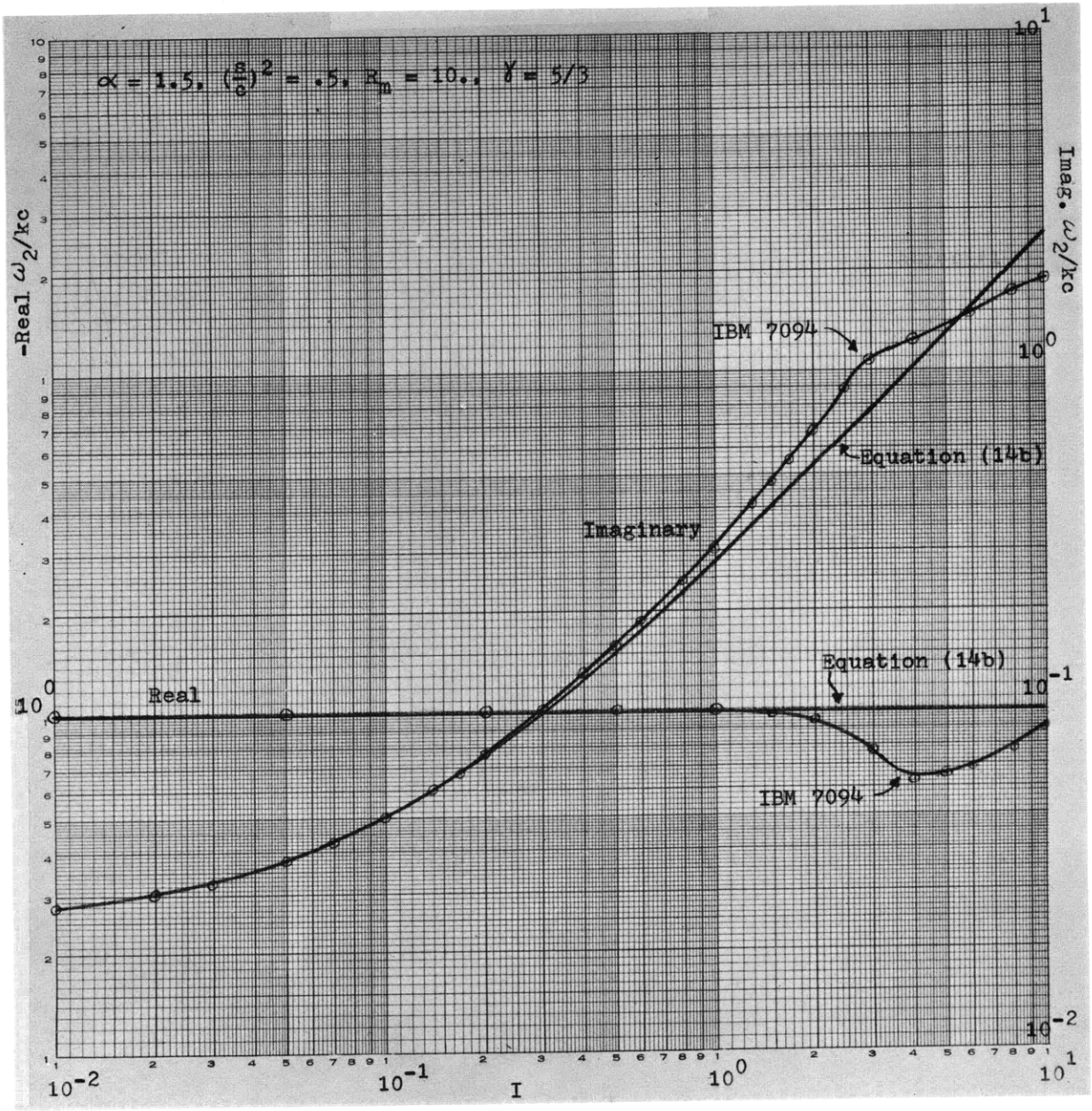

Fig. XIII-45. Comparison of Eq. 14b, for $\phi = 0$, with numerical solutions of the dispersion relation.

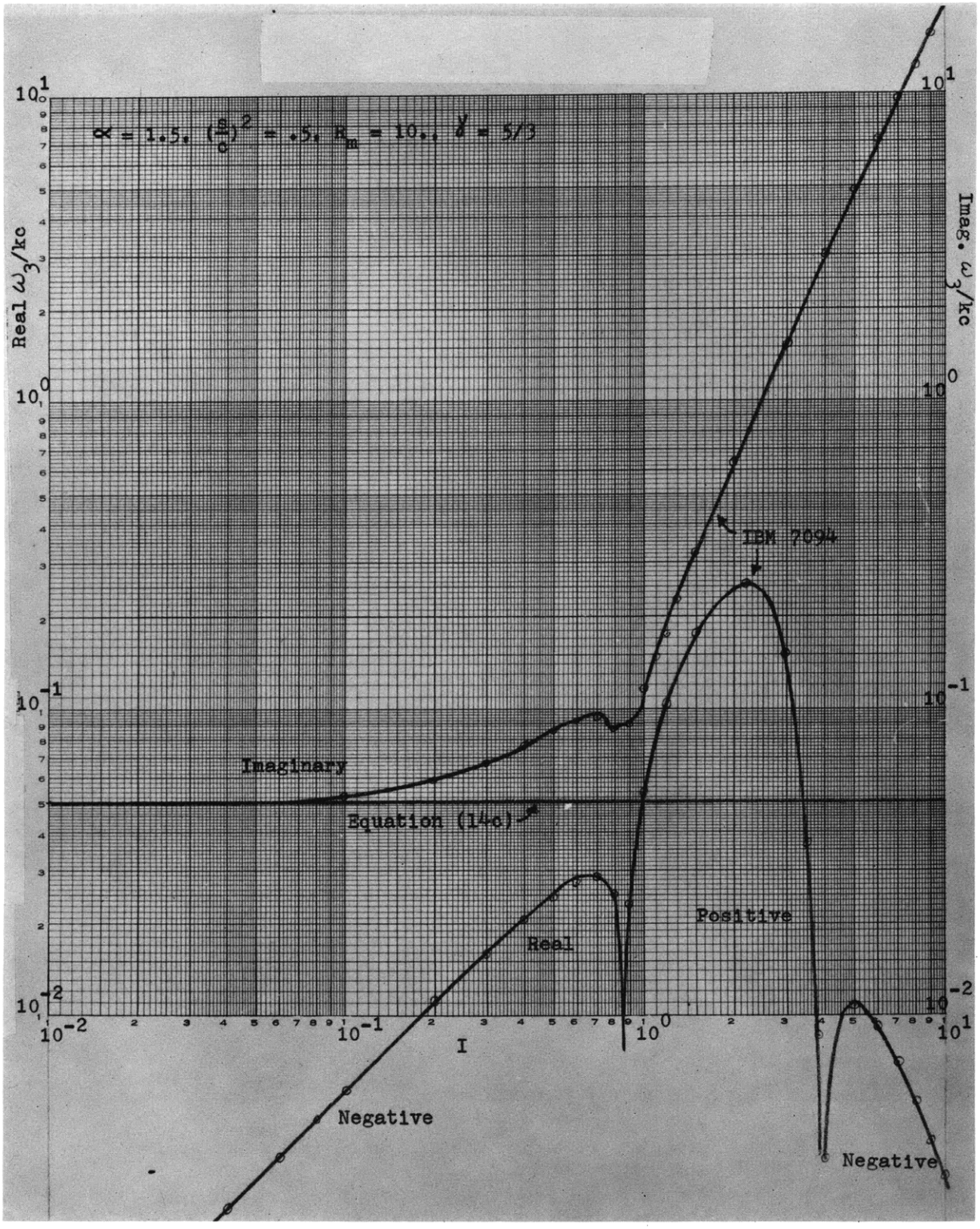

Fig. XIII-46. Comparison of Eq. 14c with numerical solutions of the dispersion relation.

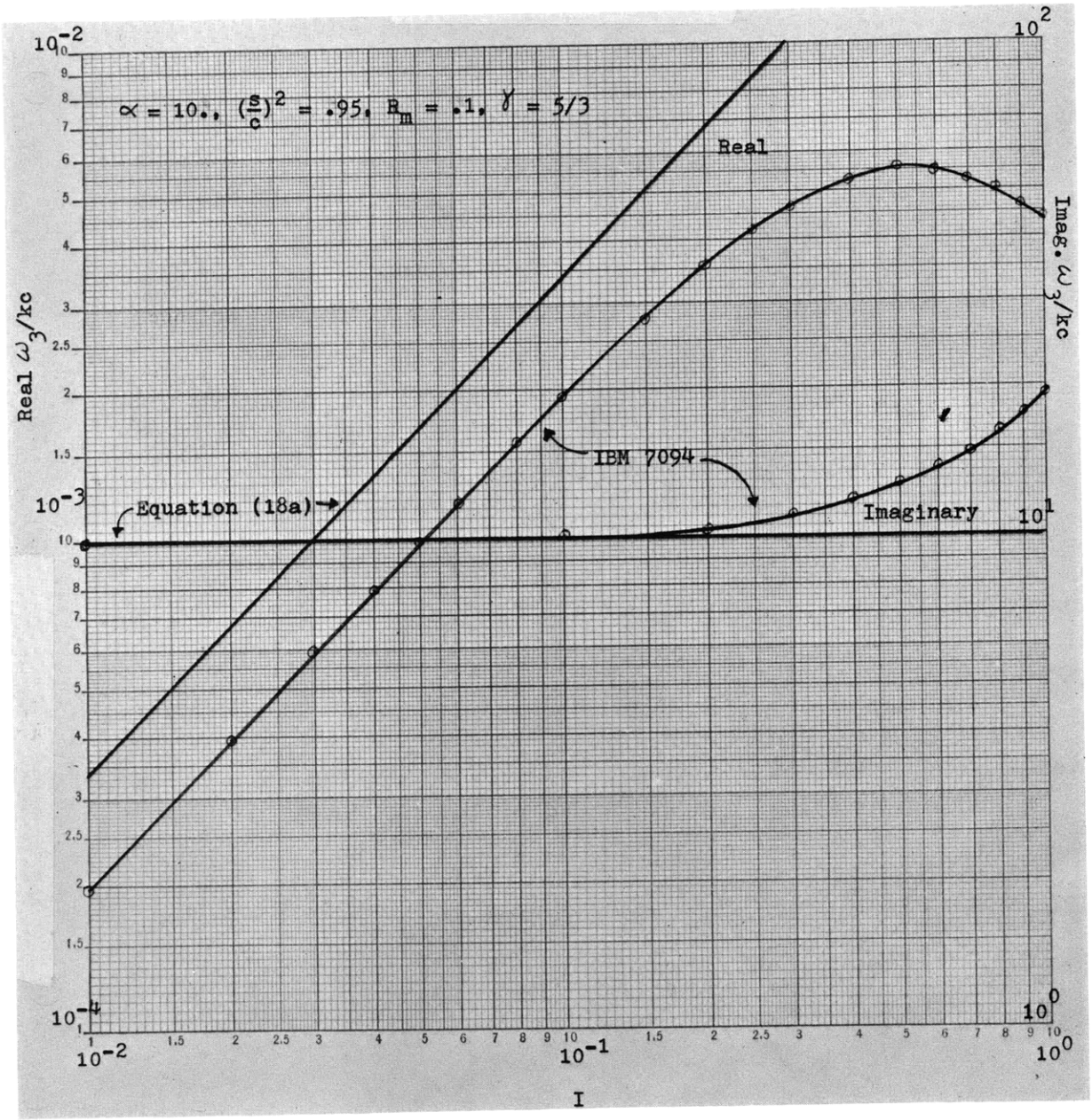

Fig. XIII-47. Comparison of Eq. 18a with numerical solutions of the dispersion relation.

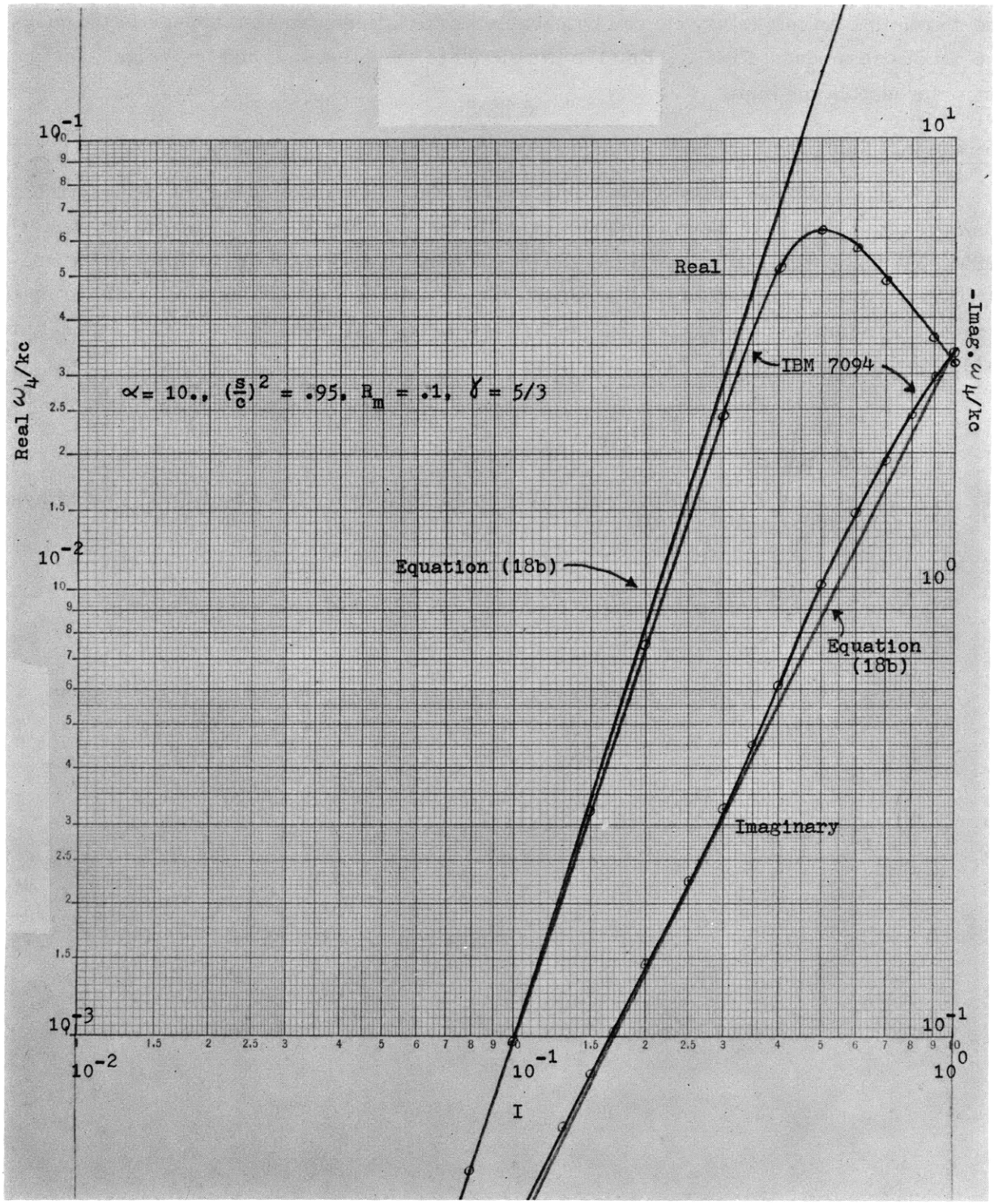

Fig. XIII-48. Comparison of Eq. 18b with numerical solutions of the dispersion relation.

be shown that an instability caused by parameter variations can also appear in the magnetoacoustic modes. Finally, Eq. 17b is related to the solution found by Wright[1] for an incompressible medium.

Numerical Solutions

The characteristic roots of the complete one-fluid dispersion equation derived from homogeneous Eqs. 2-12 were found numerically by using the M.I.T. Computation Center's IBM 7094 computer. Solutions were sought in order to ascertain the validity of the analytic descriptions presented in this report. Some critical comparisons of analytic and numerical solutions are plotted in Figs XIII-44 through XIII-48. In these figures analytic solutions are valid for $I = \mathcal{O}(0.1)$, or less.

H. A. Haus, J. E. McCune, K. R. Edwards

References

1. J. K. Wright, "A Temperature Instability in Magnetohydrodynamic Flow," Proc. Phys. Soc. (London) 81, 498 (1963).